CZECH TECHNICAL
UNIVERSITY
IN PRAGUE

FACULTY
OF ELECTRICAL
ENGINEERING

BACHELOR'S THESIS

2017

PŘEMYSL MICHAL
VIDNER

CZECH TECHNICAL UNIVERSITY IN PRAGUE

FACULTY OF ELECTRICAL ENGINEERING

Department of Electromagnetic Field

Development of Fiber Optic Gyroscope

Návrh optického vláknového gyroskopu

Bachelor's Thesis

Přemysl Michal Vidner

Supervisor: prof. Ing. Stanislav Zvánovec, Ph.D
Co-supervisor: Ing. Dmytro Suslov
Prague, May 2017

ČESKÉ VYSOKÉ UČENÍ TECHNICKÉ V PRAZE

ZADÁNÍ BAKALÁŘSKÉ PRÁCE

I. OSOBNÍ A STUDIJNÍ ÚDAJE

Příjmení: **Vidner** Jméno: **Přemysl Michal** Osobní číslo: **434886**

Fakulta/ústav: **Fakulta elektrotechnická**

Zadávající katedra/ústav: **Katedra elektromagnetického pole**

Studijní program: **Komunikace, multimédia a elektronika**

Studijní obor: **Komunikační technika**

II. ÚDAJE K BAKALÁŘSKÉ PRÁCI

Název bakalářské práce:

Návrh optického vláknového gyroskopu

Název bakalářské práce anglicky:

Development of Fiber Optical Gyroscope

Pokyny pro vypracování:

Analyzujte využití optického gyroskop na bázi vláknového Sagnacova interferometru. Navrhněte a realizujte takovýto optický gyroskop. Porovnejte přesnost a stabilitu pro provedení se standardními optickými vlákny a dále pak v případě zapojení s PM vlákny. V rámci charakterizace se následně zaměřte na využití modulátoru v rámci gyroskopu.

Seznam doporučené literatury:

[1] José Miguel López-Higuera, Handbook of Optical Fibre Sensing Technology, Wiley, 2002
[2] Agrawal

Jméno a pracoviště vedoucí(ho) bakalářské práce:

prof. Ing. Stanislav Zvánovec Ph.D., katedra elektromagnetického pole FEL

Jméno a pracoviště druhé(ho) vedoucí(ho) nebo konzultanta(ky) bakalářské práce:

Ing. Dmytro Suslov, katedra elektromagnetického pole FEL

Datum zadání bakalářské práce: **20.09.2016** Termín odevzdání bakalářské práce: **26.05.2017**

Platnost zadání bakalářské práce: **08.01.2018**

Podpis vedoucí(ho) práce	Podpis vedoucí(ho) ústavu/katedry	Podpis děkana(ky)

III. PŘEVZETÍ ZADÁNÍ

Student bere na vědomí, že je povinen vypracovat bakalářskou práci samostatně, bez cizí pomoci, s výjimkou poskytnutých konzultací. Seznam použité literatury, jiných pramenů a jmen konzultantů je třeba uvést v bakalářské práci.

.	
Datum převzetí zadání	Podpis studenta

Acknowledgements

I would like to thank Stanislav Zvánovec for the opportunity and very appreciated patient guidance, Dmytro Suslov for the much needed lab assistance, Jan Spáčil for the help with the electronics, and other guys in the lab for tolerating the mess.

I hereby declare that this thesis is my own work, and I cited all sources in accordance with Methodical Guidelines on Adherence to Ethical Policy during Higher Education Thesis Preparation.

Prohlašuji, že jsem předloženou práci vypracoval samostatně a že jsem uvedl veškeré použité informační zdroje v souladu s Metodickým pokynem o dodržování etických principů při přípravě vysokoškolských závěrečných prací.

Prague

V Praze dne:

. . . . . .

Přemysl Michal Vidner

Abstract

The first part of this thesis explores the underlying theory behind the fiber optic gyroscope – a rotation measuring device based the Sagnac interferometer. Further on, it outlines the physical effects that cause apparent sensor drift.

Most of this work describes design process of such a device with focus on phase modulation setting and sensor drift reduction. The final gyroscope is comprised of a 998 m long single-mode fiber spool, an erbium-doped fiber based light source, two fiber-optic couplers, optoelectric phase modulator, and signal processing electronics.

The figures of merit of the resulting device are these: Random walk $5.18\,^{\circ}/\sqrt{\mathrm{h}}$, Bias instability $1.37\,^{\circ}/\mathrm{h}$, Lowest detectable rate $0.70\,^{\circ}/\mathrm{h}$, Scale factor $7.38\,^{\mathrm{deg/s}}/\mathrm{V}$.

Abstrakt

První část této práce zkoumá teorii stojící za optickým vláknovým gyroskopem, což je zařízení fungující na bázi Sagnacova interferometru k měření rotace. Teoretická část dále popisuje fyzikální jevy, které způsobují zjevnou nestabilitu těchto sensorů.

Druhá část práce popisuje postup návrhu takového zařízení. Zaměřujeme se obzvláště na nastavení fázové modulace a zvýšení stability sensoru. Výsledný gyroskop je sestaven z 998 m dlouhé špulky jednovidového optického vlákna, ze zdroje záření založeném na erbiem dotovaném vlákně, z dvou optických vazebných členů, z optoelektrického fázového modulátoru a z vyhodnocovací elektroniky.

Výsledné parametry gyroskopu jsou: Random walk (míra šumu) $5,18\,^{\circ}/\sqrt{\mathrm{h}}$; Bias instability (míra dlouhodobé nestability) $1,37\,^{\circ}/\mathrm{h}$; nejnižší detekovatelná rotace $0,70\,^{\circ}/\mathrm{h}$; citlivost $7,38\,^{\circ}/\mathrm{s}/\mathrm{V}$.

Keywords

fiber optic gyroscope, rotation sensing, interferometry, Sagnac effect, sensor drift, phase modulation, Allan variance

Klíčová slova

optický vláknový gyroskop, měření rotace, interferometrie, Sagnacův efekt, drift senzoru, fázová modulace, Allanův rozptyl

Contents

Nomenclature

Quantities

Quantity	Dimension	
B	$^{\text{rad}}/_{\text{s}}$	Bias instability
c	$299\,792\,458\,^{\text{m}}/_{\text{s}}$	Speed of light
E	$^{\text{V}}/_{\text{m}}$	**E**-field magnitude
f_m	Hz	Modulating signal frequency
ϕ	rad	Wave-front phase
ϕ_S	rad	Sagnac phase shift
h	-	Phase modulation index
j	$\sqrt{-1}$	Imaginary unit
L	m	Fiber spool length
λ	m	Wavelength in medium
λ_0	m	Wavelength in vacuum
n	-	Refractive index
N	-	Number of loops
r	m	Radius of the fiber loop
RW or N	$^{\text{rad}}/_{\sqrt{\text{s}}}$	Random walk
S	$\frac{\text{V}}{^{\text{rad}}/_{\text{s}}}$	Gyro sensitivity
V_m	V	Modulation voltage
V_o	V	Output voltage
ω_m	$^{\text{rad}}/_{\text{s}}$	Modulating signal ang. velocity
Ω	$^{\text{rad}}/_{\text{s}}$	Angular velocity of rotation

Using SI units
Positive angular velocity represents counter-clockwise rotation according to right-hand rule

Abbreviations

CW	Clockwise
CCW	Counter-clockwise
ED(F)	Erbium-doped (fiber)
EDFA	Erbium-doped fiber amplifier
ERS	Earth's rotation speed
Φ	Phase modulator
FFT	Fast Fourier transform
FOG	Fiber optic gyroscope
MSE	Mean squared error
OTDR	Optical time-domain reflectometry
PM(F)	polarization-maintaining (fiber)
SLED	Superluminescent light-emitting diode
SM(F)	Single-mode (fiber)

Rotational speed units

From ↓ \ To →	rad/s	rpm	deg/s	deg/h	ERS	Hz
1 rad/s	1	9.55	57.3	206300	13800	0.159
1 rpm	0.105	1	6	1440	1440	0.0167
1 deg/s	0.0175	0.167	1	240	240	0.00278
1 deg/h	$4.85 \cdot 10^{-6}$	$4.63 \cdot 10^{-5}$	$2.78 \cdot 10^{-4}$	1	0.0667	$7.72 \cdot 10^{-7}$
ERS	$7.25 \cdot 10^{-5}$	$6.94 \cdot 10^{-4}$	0.00417	15	1	$1.16 \cdot 10^{-5}$
1 Hz	6.28	60	360	$1.30 \cdot 10^{-6}$	86200	1

Introduction

The fiber optic gyroscope is a direct application of the Sagnac interferometer. A light beam is split in two and enters a ring (needn't be circular). Both beams travel the same path. Any rotation induced results in a phase shift of the recombined incident beam, which can be detected as an interference pattern (free space) or current in a photodiode (fiber).

A gyroscope built upon fiber optics offers several advantages as a rotation measuring device: it is a fully solid state device, hence it isn't subject to mechanical wear and can be ruggedized. Its sensitivity can be fairly simply adjusted by the number of its fiber loops – easily allowing sensitivities to detect Earth's rotation rate. State of the art fiber gyroscopes are extremely precise measuring instruments, that are applied as inertial navigation units in aircraft and space vehicles.

A basic fiber optic setup includes a fairly long fiber (about 1 km in our case) wound into a coil, two fiber couplers, a source, and a detector. One arm of the interferometer also has a phase modulator in its path. The phase modulation allows to distinguish the sense of rotation and maximizes the sensitivity of the gyro.

A major hindrance in the optical domain to overcome is the drift of the sensor. A naïve implementation of the basic fiber setup results in a very significant drift. Therefore several improvements are required in order to minimize the temperature drift, polarization drift, and Kerr drift.

The first part describes the underlying principles of the gyroscope – the Sagnac effect and the basic fiber gyroscope setup, including phase modulation. Further on, we deal with sensor drift, its sources and ways of reducing it.

The second part describes development of a single axis fiber gyroscope prototype, ultimately for aerospace application. We begin with a simple setup, deal with sensor drift, improve accuracy, and end up with Earth's rotation rate sensitivity gyro.

Part 1

Theory

1.1 The Sagnac effect

The operating principle of any optical gyroscope is the Sagnac effect: an optical interference caused by differing optical path lengths of a split beam traveling in opposite directions in a rotating ring.

Consider the arrangement in Fig. 1.1 on the following page: a beam is split in two by the beam splitter (a 2×2 fiber coupler in our case). Both beams travel the same optical path but in opposite directions. Should the interferometer rotate, the path length changes but the propagation speed does not. If the interferometer rotates counter-clockwise, the path of counter-clockwise (CCW) propagating beam (a^+) gets longer and the path of clockwise (CW) beam (a^-) gets shorter during the travel time. The reference point moves by Δl, which is the path difference. The consequence is that the beams arrive to the detector with a phase shift, hence the interference.

This simplified understanding doesn't apply when the light propagates in a medium (e.g. single-mode fiber), but the resulting interference is, however, the same irrespective of the propagation speed, as will be shown further on.

1.1.1 Derivation

Let us consider a wave traveling in a hypothetical circular vacuum waveguide. The time of travel is

$$t = \frac{2\pi r N + \Delta l}{c}. \tag{1.1}$$

r is the coil radius, N is the number of coil loops, Δl is the path length change caused by the rotation (angular velocity Ω).

$$\Delta l = \pm \Omega r t. \tag{1.2}$$

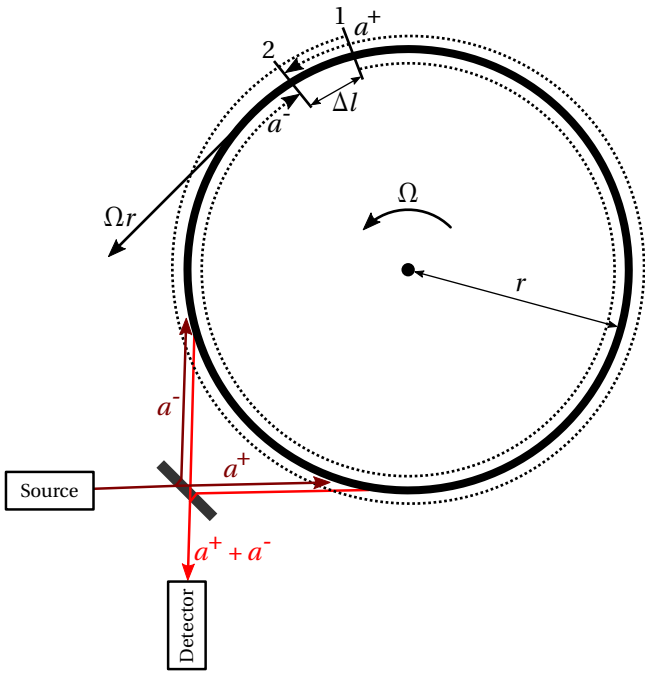

Figure 1.1: Principle of the Sagnac Effect.

The path length change of the wave propagating in the same direction as the rotation is positive (longer path), Δl of the counter-propagating wave is negative (shorter path). This gives

$$t^+ = \frac{2\pi rN + \Omega r t^+}{c} = \frac{2\pi rN}{c - \Omega r}, \tag{1.3}$$

$$t^- = \frac{2\pi rN - \Omega r t^-}{c} = \frac{2\pi rN}{c + \Omega r}. \tag{1.4}$$

The time difference is

$$\delta t = \left| t^+ - t^- \right| = \frac{4\pi r^2 N\Omega}{\Omega^2 r^2 - c^2}. \tag{1.5}$$

Considering $\Omega^2 r^2 \ll v^2$,

$$\delta t \approx \frac{4\pi r^2 N\Omega}{c^2}, \tag{1.6}$$

which is also the first term in the Taylor series. The total path difference relative to both beams (speed of propagation remaining constant) is

$$\delta d = c\delta t = \frac{4\pi r^2 N\Omega}{c}. \tag{1.7}$$

In terms of phase shift, we obtain the formula for the Sagnac interference in a vacuum waveguide [1, 2, 3]:

$$\phi_S = \frac{2\pi\delta d}{\lambda_0} = \frac{8\pi^2 r^2 N\Omega}{c\lambda_0}. \tag{1.8}$$

Sometimes, it is more practical to express the phase shift in terms of the length of the waveguide rather than the number of the loops:

$$\begin{aligned} N(L,r) &= \frac{L}{2\pi r} \\ \phi_S &= \frac{4\pi r L\Omega}{c\lambda_0}. \end{aligned} \tag{1.9}$$

1.1.2 Fizeau drag

Propagation speed in a dielectric waveguide is substantially lower than in vacuum. In this case we assume it's c/n, where n is the refractive index of the medium. Moreover, a lightwave traveling in a moving medium is dragged by it. The effect is known as the Fizeau drag, and can be explained by relativistic addition of velocities.

We shall now demonstrate that the Sagnac phase shift isn't affected by the refractive index of the medium because the effects of sumbluminal phase velocity and relativistic frame dragging cancel each other out. Arditty and Lefèvre [1] demonstrate it with regard to Fizeau's experimental results, we will use relativistic addition of velocities.

The relativistic velocity addition formula in one spatial dimension for collinear motion (supposing wavelengths negligible in comparison with coil radius) is as follows [4]:

$$u \oplus v \equiv \frac{u+v}{1+\frac{uv}{c^2}}. \tag{1.10}$$

The phase velocity of the wave propagating in the same direction as the rotation adds up with the tangential speed of rotation and vice versa:

$$\begin{aligned} v^+ &= \frac{c}{n} \oplus \Omega r = \frac{\frac{c}{n}+\Omega r}{1+\frac{\Omega r}{cn}} \\ v^- &= \frac{c}{n} \oplus (-\Omega r) = \frac{\frac{c}{n}-\Omega r}{1-\frac{\Omega r}{cn}}. \end{aligned} \tag{1.11}$$

As with the hypothetical vacuum waveguide, the path length changes as a result of the rotation. Substituting c with v^+ and v^- in equations 1.3 and 1.4 on the preceding page gives

$$\begin{aligned} t^+ &= \frac{2\pi r N(cn+\Omega r)}{-c^2+\Omega^2 r^2} \\ t^- &= \frac{2\pi r N(-cn+\Omega r)}{-c^2+\Omega^2 r^2}. \end{aligned} \tag{1.12}$$

Total distance traveled for both waves is

$$\begin{aligned} d^+ &= v^+ t^+ = \frac{2\pi r N c\,(c + n\Omega r)}{c^2 - \Omega^2 r^2} \\ d^- &= v^- t^- = \frac{2\pi r N c\,(c - n\Omega r)}{c^2 - \Omega^2 r^2}. \end{aligned} \tag{1.13}$$

Their actual wavelengths in the medium are $\lambda^\pm = \frac{v^\pm}{c}\lambda_0$, so their phases are $\phi^\pm = \frac{2\pi d^\pm}{\lambda^\pm}$. Finally, we can obtain the phase shift:

$$\begin{aligned} \Delta\phi_\mathrm{m} = \left|\phi^+ - \phi^-\right| &= \left| \frac{2\pi}{\frac{c}{n}\oplus\Omega r}\lambda_0 \frac{2\pi r N c\,(c + n\Omega r)}{c^2 - \Omega^2 r^2} - \frac{2\pi}{\frac{c}{n}\oplus(-\Omega r)}\lambda_0 \frac{2\pi r N c\,(c - n\Omega r)}{c^2 - \Omega^2 r^2} \right| = \\ &= \left| \frac{4\pi^2 r c\,(cn + \Omega r)}{\lambda_0\left(c^2 - \Omega^2 r^2\right)} - \frac{4\pi^2 r c\,(cn - \Omega r)}{\lambda_0\left(c^2 - \Omega^2 r^2\right)} \right| = \frac{8\pi^2 r^2 c\Omega}{\lambda_0\left(c^2 - \Omega^2 r^2\right)}. \end{aligned} \tag{1.14}$$

The first term in the Taylor power series ($\Omega_0 = 0$) gives the same result as the hypothetical vacuum waveguide –

$$\Delta\phi_\mathrm{m} \approx \frac{8\pi^2 r^2 \Omega}{c\lambda_0} = \phi_\mathrm{S}. \tag{1.15}$$

Therefore the Sagnac effect is independent on the medium of propagation in a circular path. More rigorous and complex proof based on Maxwell's equations rather than relativistic kinematics is given by Arditty and Lefèvre [1]. The results are the same.

1.2 Interferometric setup

1.2.1 S-parameter matrices

We shall describe the FOG as a two port network in terms of signal amplitude (**E** or **B** field) neglecting backreflections.

1.2.1.1 2×2 fiber coupler

The optical coupler is essentially a pair of fibers with conveniently fused claddings. The principle is that an incoming lightwave splits in two via evanescent wave coupling (coupling ratio $\alpha = \frac{P_1}{P_1+P_2}$). The S-matrix for a bidirectional 2×2 coupler is as follows [5] –

$$\mathrm{S}_\mathrm{cpl} = \begin{bmatrix} \sqrt{1-\alpha} & j\sqrt{\alpha} \\ j\sqrt{\alpha} & \sqrt{1-\alpha} \end{bmatrix}. \tag{1.16}$$

$\sqrt{1-\alpha}$ is amplitude coupling ratio, $j\sqrt{\alpha}$ is phase shift.

For a 50% coupler ($\alpha = 0.5$), we get

$$\mathrm{S_{cpl}} = \begin{bmatrix} \frac{\sqrt{2}}{2} & j\frac{\sqrt{2}}{2} \\ j\frac{\sqrt{2}}{2} & \frac{\sqrt{2}}{2} \end{bmatrix}. \tag{1.17}$$

1.2.1.2 Fiber loop

We need to describe both terminals of the Sagnac loop in terms of the absolute phase of both phase-shifted waves. Applying equations 1.3 and 1.4 on page 16 –

$$\begin{aligned} t_{1,2} &= \frac{2\pi r N}{c \mp \Omega r}, \\ d_{1,2} &= \frac{2\pi c r N}{c \mp \Omega r}, \\ \phi_{1,2} &= \frac{2\pi d_{1,2}}{\lambda_0} = \frac{4\pi^2 c r N}{\lambda_0 (c \mp \Omega r)}. \end{aligned} \tag{1.18}$$

The phase shift applied within the section is simply multiplication by $e^{-j\phi}$, therefore

$$\mathrm{S_{sag}} = \begin{bmatrix} 0 & e^{-j\phi_2} \\ e^{-j\phi_1} & 0 \end{bmatrix} = \begin{bmatrix} 0 & \exp\left(\frac{-j4\pi^2 c r N}{\lambda_0 (c+\Omega r)}\right) \\ \exp\left(\frac{-j4\pi^2 c r N}{\lambda_0 (c-\Omega r)}\right) & 0 \end{bmatrix}. \tag{1.19}$$

1.2.2 Network function

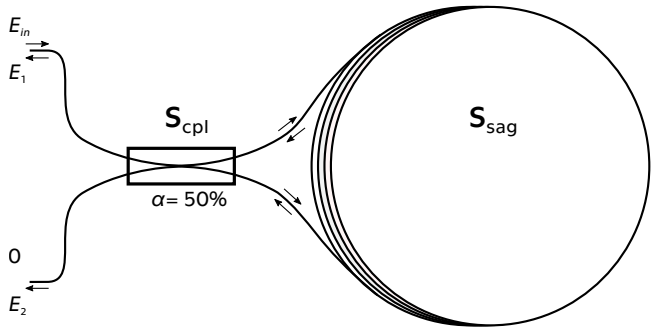

Figure 1.2: Sagnac interferometer – fundamental fiber setup

Let us analyze the basic fiber Sagnac interferometer as shown in Fig. 1.2:

$$
\begin{aligned}
\begin{bmatrix} E_1 \\ E_2 \end{bmatrix} &= \mathrm{S_{cpl}} \cdot \mathrm{S_{sag}} \cdot \mathrm{S_{cpl}} \cdot \begin{bmatrix} E_{\mathrm{in}} \\ 0 \end{bmatrix} \\
\begin{bmatrix} E_1 \\ E_2 \end{bmatrix} &= \begin{bmatrix} \frac{\sqrt{2}}{2} & j\frac{\sqrt{2}}{2} \\ j\frac{\sqrt{2}}{2} & \frac{\sqrt{2}}{2} \end{bmatrix} \cdot \begin{bmatrix} 0 & e^{-j\phi_2} \\ e^{-j\phi_1} & 0 \end{bmatrix} \cdot \begin{bmatrix} \frac{\sqrt{2}}{2} & j\frac{\sqrt{2}}{2} \\ j\frac{\sqrt{2}}{2} & \frac{\sqrt{2}}{2} \end{bmatrix} \cdot \begin{bmatrix} E_{\mathrm{in}} \\ 0 \end{bmatrix} \\
\begin{bmatrix} E_1 \\ E_2 \end{bmatrix} &= \begin{bmatrix} \frac{1}{2} j \left(e^{-j\phi_1} + e^{-j\phi_2} \right) E_{\mathrm{in}} \\ \frac{1}{2} \left(e^{-j\phi_1} - e^{-j\phi_2} \right) E_{\mathrm{in}} \end{bmatrix} \\
\begin{bmatrix} E_1 \\ E_2 \end{bmatrix} &= \begin{bmatrix} \frac{1}{2} j \left(e^{-j\left(\frac{\phi_1+\phi_2}{2} + \frac{\phi_1-\phi_2}{2}\right)} + e^{-j\left(\frac{\phi_1+\phi_2}{2} - \frac{\phi_1-\phi_2}{2}\right)} \right) E_{\mathrm{in}} \\ \frac{1}{2} \left(e^{-j\left(\frac{\phi_1+\phi_2}{2} + \frac{\phi_1-\phi_2}{2}\right)} - e^{-j\left(\frac{\phi_1+\phi_2}{2} - \frac{\phi_1-\phi_2}{2}\right)} \right) E_{\mathrm{in}} \end{bmatrix}.
\end{aligned}
\tag{1.20}
$$

Substituting phase difference yields Sagnac phase shift (Eq. 1.8 on page 17).

$$
\Delta\phi = \phi_1 - \phi_2 = \frac{4\pi^2 crN}{\lambda_0 (c - \Omega r)} - \frac{4\pi^2 crN}{\lambda_0 (c + \Omega r)} = \frac{8\pi^2 r^2 cN\Omega}{c^2\lambda_0 - \lambda\Omega^2 r^2} \approx \frac{8\pi^2 r^2 N\Omega}{c\lambda_0} = \phi_S.
\tag{1.21}
$$

The equation can be further simplified by substituting average phase shift $\phi_0 = \frac{\phi_1+\phi_2}{2}$;

$$
\begin{aligned}
\begin{bmatrix} E_1 \\ E_2 \end{bmatrix} &= \begin{bmatrix} \frac{1}{2} j \left(e^{-j\left(\phi_0 + \frac{1}{2}\Delta\phi\right)} + e^{-j\left(\phi_0 - \frac{1}{2}\Delta\phi\right)} \right) E_{\mathrm{in}} \\ \frac{1}{2} \left(e^{-j\left(\phi_0 + \frac{1}{2}\Delta\phi\right)} - e^{-j\left(\phi_0 - \frac{1}{2}\Delta\phi\right)} \right) E_{\mathrm{in}} \end{bmatrix} \\
\begin{bmatrix} E_1 \\ E_2 \end{bmatrix} &= \begin{bmatrix} j e^{-j\phi_0} \left(\frac{1}{2} e^{-j\frac{1}{2}\Delta\phi} + \frac{1}{2} e^{j\frac{1}{2}\Delta\phi} \right) E_{\mathrm{in}} \\ -j e^{-j\phi_0} \left(\frac{1}{2} j e^{-j\frac{1}{2}\Delta\phi} - \frac{1}{2} j e^{j\frac{1}{2}\Delta\phi} \right) E_{\mathrm{in}} \end{bmatrix} \\
\begin{bmatrix} E_1 \\ E_2 \end{bmatrix} &= \begin{bmatrix} j e^{-j\phi_0} \cos\left(\frac{\Delta\phi}{2}\right) E_{\mathrm{in}} \\ -j e^{-j\phi_0} \sin\left(\frac{\Delta\phi}{2}\right) E_{\mathrm{in}} \end{bmatrix}.
\end{aligned}
\tag{1.22}
$$

So are power network functions obtained from the result:

$$
\begin{aligned}
P_{11} &= \left| \frac{E_1}{E_{\mathrm{in}}} \right|^2 = \cos^2\left(\frac{\phi_S}{2}\right), \\
P_{12} &= \left| \frac{E_2}{E_{\mathrm{in}}} \right|^2 = \sin^2\left(\frac{\phi_S}{2}\right).
\end{aligned}
\tag{1.23}
$$

It is desirable to utilize the output at the input port $\left(P_{11} = \cos^2\left(\frac{\phi_S}{2}\right)\right)$ as explained by Ruffin [3]: The P_{12} output is not reciprocal because the constituent waves of the recombined signal do not travel the same path. The CW propagating wave is coupled twice by the coupler, while the CCW wave is transmitted twice by the coupler. This induces another phase shift, indistinguishable from the desired Sagnac phase shift.

Measuring P_{11} requires an additional coupler, see Fig. 1.3 for the scheme. It is reasonable to assume the output would be the same, only the signal's

power would be four-fold attenuated, because half of the power is discarded twice at the couplers. This is indeed the case, the network function can be derived the same way as above:

$$P_{out} = \left| \frac{E_b}{E_{in}} \right|^2 = \frac{1}{4} \cos^2 \left(\frac{\phi_S}{2} \right). \tag{1.24}$$

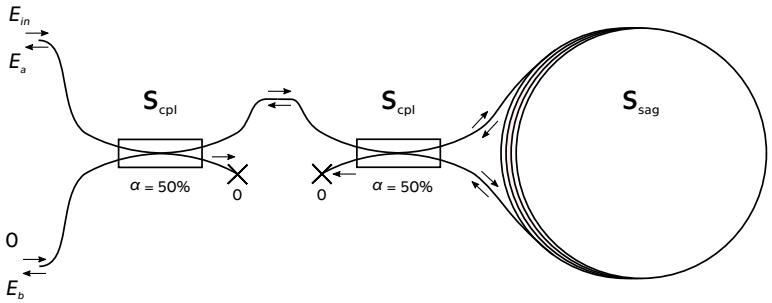

Figure 1.3: Fiber optic gyroscope – basic setup utilizing the reciprocal port

1.2.3 Phase modulation

Let us examine the sensitivity of the bare P_{11} output.

$$\frac{dP_{11}}{d\phi_S} = -\frac{1}{2} \sin \phi_S, \tag{1.25}$$

this means the slope, consequently sensitivity, of the output function is zero with no Sagnac phase shift. The sensitivity can be adjusted by essentially biasing the gyro by modulating the phase of the optical signal by a carrier frequency ω_0. The physical interpretation is that both waves experience different phase shift at the modulator, because they encounter it at different times: one wave as soon as it enters the Sagnac loop, the other as it leaves the loop.

The output function can be expressed

$$P_{11} = \cos^2 \left(\frac{\phi_S}{2} \right) = \frac{1}{2} \left(\cos \left(\phi_S \right) + 1 \right). \tag{1.26}$$

Applying sinewave modulation with modulation depth h and modulation frequency ω_0 yields

$$P_m = \frac{1}{2} \left(\cos \left(\phi_S + h \sin \omega_0 t \right) + 1 \right). \tag{1.27}$$

To assess the output we need to obtain the prescription for the harmonics, so we expand the function into its Bessel series [2]:

$$P_m = \frac{1}{2} \left(J_0(h) \cos \left(\phi_S \right) + 1 \right) + \sum_{n=1}^{\infty} J_{2n}(h) \cos(2n\omega_0 t) \cos \phi_S - \sum_{n=1}^{\infty} J_{2n-1}(h) \sin((2n-1)\omega_0 t) \sin \phi_S. \tag{1.28}$$

As it can be seen, the even harmonics carry sine dependence while odd harmonics are still cosine. The slope, or derivative, of the sine harmonics has indeed a maximum at $\phi_S = 0$. The first even harmonic is the strongest one:

$$P_m \approx J_1(h) \sin(\omega_0 t) \sin\phi_S. \tag{1.29}$$

To maximize this particular term, we need to set the modulation depth so that the Bessel function $J_1(h)$ is at its maximum:

$$\max\{J_1(h)\} \approx J_1(1.841). \tag{1.30}$$

The optimal modulation frequency is equal to the eigenfrequency of the gyroscope [3, 6]

$$f_\lambda = \frac{c}{2nL}, \tag{1.31}$$

where L is total fiber length. The eigenfrequency corresponds to the time of light's travel in the fiber spool. If the period of the modulating signal is equal to the travel time, both CW and CCW waves encounter the same phase shift at the modulator when the gyro is still.

1.3 Parasitic phase shift

In practice, the Sagnac effect is not the only source of measurable phase shift. These effects generally stem from any nonreciprocal change of optical path, and are undistinguishable from Sagnac phase shift, hence very much undesirable.

We shall present an overview of these effects and possible ways to reduce them.

1.3.1 Polarization effects

If the polarization states of interfering waves differ, so does the resulting interference [5]. If the difference in polarization changes over time a sensor drift is detected.

The first cause of polarization induced drift is random birefringence along the fiber due to stress and temperature [3]. If the permittivity tensor changes over time at a particular location in the fiber loop, the CW and CCW waves experience a different net rotation of the polarization planes, because they encounter the spot at different times. Gradual change of birefringent properties results in sensor drift.

Differential rotation of the polarization planes can also be induced by Faraday effect [3], that is a rotation in presence of a magnetic field. This can be naturally also reduced by shielding the gyroscope.

Conveniently enough, these polarization effects can be reduced in a fiber with linear and well-defined birefringence (polarization-maintaining

/PM/ fiber) [2, 6]. However, polarization axes of a PM coupler (plus connectors and welds of course) are never perfectly aligned. This leads polarization mode coupling [7], which results in an additional undesired interference. The mode coupling depends on light coherence, which means a broadband light source should reduce this effect [3, 6, 7].

1.3.2 Nonlinear effects

Nonlinear effects that cause nonreciprocities in the FOG are caused by the optical Kerr effect. That is a third order nonlinearity that makes refractive index dependent on light intensity [8]:

$$n = n_0 + n_2 I = n_0 + \frac{6\pi}{n_0}\chi^{(3)}\left|E(\omega)\right|^2 \tag{1.32}$$

n_2 is general nonlinear refractive index and I beam intensity (W/m^2). $\chi^{(3)}$ is third-order nonlinear optical susceptibility – generally a fourth-rank tensor (i.e. 81 separate elements).

Intensity-dependent refractive index results in several processes, the one responsible for parasitic phase shift in the FOG is four-wave mixing between the counterpropagating waves [6]. This is a complex process beyond the scope of this work, but rudimentary explanation can be done via cross-phase modulation [7]:

The change in refractive index due to Kerr effect of a wave itself is

$$\Delta n_+ = n_2 I_1. \tag{1.33}$$

The change in refractive index due to the counterpropagating wave is twice as strong [8][7]:

$$\Delta n_x = 2 n_2 I_2. \tag{1.34}$$

Hence phase shifts due to both contributions are [7]:

$$\Delta\phi_+ = \frac{2\pi n_2 L}{\lambda}\frac{P_+}{A} \quad \Delta\phi_x = \frac{4\pi n_2 L}{\lambda}\frac{P_x}{A}, \tag{1.35}$$

where L is optical path length, A is effective aperture, P_+ and P_x are powers of propagating and counterpropagating waves.

Should the powers of the CW and CCW waves be different, phase shift occurs [7]:

$$\Delta\phi_{CW} = \frac{2\pi n_2 L}{\lambda A}\left(P_{CW} + 2P_{CCW}\right) \quad \Delta\phi_{CCW} = \frac{2\pi n_2 L}{\lambda A}\left(2P_{CW} + P_{CCW}\right) \tag{1.36}$$

$$\Delta\phi_{Kerr} = \left|\Delta\phi_{CW} - \Delta\phi_{CCW}\right| = \frac{2\pi n_2 L}{\lambda A}\Delta P \tag{1.37}$$

The issue is that any change in power difference of the CW and CCW waves causes drift, and the change needn't be large: even change in order

of microwatts may cause drift of single degrees per hour in an average gyroscope [7]. The solution to this problem is either reducing input power or using incoherent light instead of a laser source [2, 3, 6, 7]. The reason for using broadband source is that it consists of many frequency components, therefore the change due to Kerr effect is mostly caused by other frequency components $(\Delta\phi_x)$, which means $\Delta\phi_+$ plays little role, and the nonreciprocity vanishes.[7]

1.3.3 Shupe effect

Refractive index is dependent on temperature and mechanical stress.[9] Should the temperature and stress remain constant, the gyro remains reciprocal. However, should there be a time-gradient in temperature and/or stress, the optical path lengths of the counterpropagating waves differ, hence a phase shift. The nonreciprocity can be explained by the fact that each wave encounters a different change in refractive index, because a thermal or stress event, located at a particular spot of the fiber spool, changes magnitude before the second wave arrives.

The Shupe effect due to thermal gradient in the FOG can be described as follows [3] –

$$\Delta\phi_{Sh} = \frac{2\pi c}{\lambda n}\left(\frac{\partial n}{\partial \vartheta} + \alpha n\right)\int_0^{L/2} (2l - L)\left(\frac{\partial \vartheta}{\partial t}(l) - \frac{\partial \vartheta}{\partial t}(L - l)\right) dl \tag{1.38}$$

ϑ	Temperature
α	Thermal expansion coefficient of the fiber
L	Fiber length
l	Location of an infinitesimal thermal event

Since the thermal gradient is almost always nonzero under usual conditions, Shupe effect leads to sensor drift.

The obvious solution is mechanical (e.g. encasing the spool in epoxy resin) and thermal stabilization. The less obvious solution is winding the spool in a particular way so that thermal and stress gradients are encountered reasonably evenly by both waves.[3, 7]

Basic winding methods are unipolar, dipolar, and quadrupolar winds [3]. Unipolar (end-to-end) wind is the basic helix winding method, it doesn't mitigate Shupe effect. Shupe effect can be reduced by winding the coil from the center of the fiber, unlike the simple wind. See Fig. 1.4 on the next page for actual winding schemes of the dipolar and quadrupolar wind. Dipolar wind mitigates the Shupe effect by $1/N_L$ quadrupolar by $1/N_L^2$, where N_L is the number of fiber layers wound around the mandrel [3].

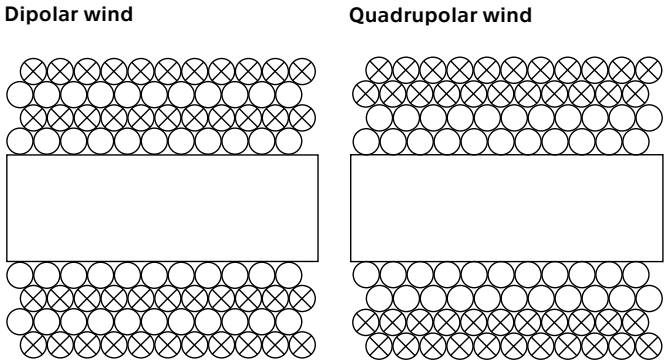

Figure 1.4: Center-to-end winds according to Ruffin [3] and Lefèvre [6].

1.4 State of the art

There are further possible improvements apart from those previously suggested.

High performance gyros require much greater dynamic range than it is possible with the open-loop configuration. This can be achieved via closed-loop (i.e. feedback) signal processing scheme. The demodulated biased signal is used as an error signal that is fed back into the system to generate an additional feedback phase difference that is maintained opposite to the Sagnac phase [6]. In essence, the feedback loop nulls the Sagnac phase shift and keeps the gyro within its linear range.

There are several methods of implementing the feedback scheme [3, 7, 6], a basic one [2, 6] is shown in Fig. 1.5 on the following page. The microprocessor generates an error signal based on detected power change. The error signal adds up with the basic modulation signal and cancels out the Sagnac phase shift. Rotation rate is measured indirectly through the error signal, unlike the open-loop configuration which measures the phase shift itself.

Another improvement is implementing the couplers and modulator on a single integrated planar optics chip. The integrated optics allows for a better broadband push-pull modulator and greater polarization extinction ratio (further reducing polarization induced drift) [7].

The performance of gyroscopes is usually measured in bias instability B – the measure of drift performance and random walk RW – the measure of noise performance. A convenient benchmark for bias instability is Earth's rotation rate of $15\,^{\mathrm{deg}}/_{\mathrm{h}}$. Some FOGs available on the market spanning from relatively cheap ones to bleeding-edge technology are presented in Tab. 1.1 on the next page.

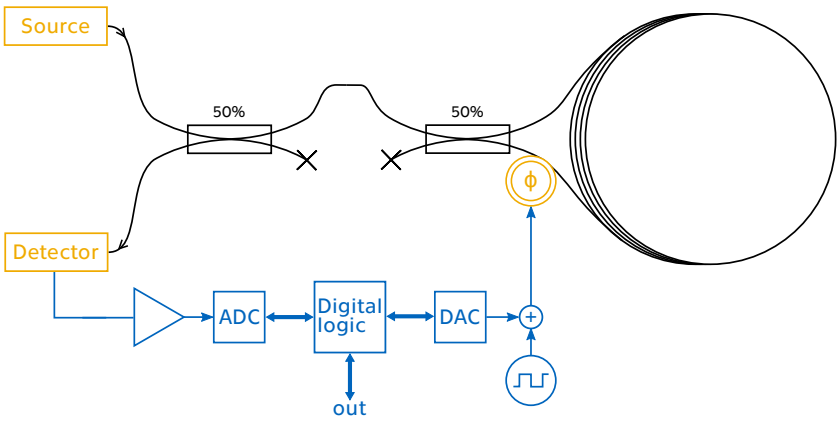

Figure 1.5: A basic closed loop configuration after Merlo et al. [2]

Model	Manufacturer	Random Walk	Bias instability	Application
DSP-3000 [10]	KVH	$0.067\,^{\mathrm{deg}}/\sqrt{\mathrm{h}}$	$1\,^{\mathrm{deg}}/\mathrm{h}$	Stabilization
8088 [11]	Saab	$0.05\,^{\mathrm{deg}}/\sqrt{\mathrm{h}}$	$1\,^{\mathrm{deg}}/\mathrm{h}$	Naval
EMP-1 [12]	Emcore	$0.015\,^{\mathrm{deg}}/\sqrt{\mathrm{h}}$	$0.5\,^{\mathrm{deg}}/\mathrm{h}$	UAV & robotics
FOG 53 [13]	Al Cielo	$0.001\,^{\mathrm{deg}}/\sqrt{\mathrm{h}}$	$0.005\,^{\mathrm{deg}}/\mathrm{h}$	Aerospace
Astrix-200 [14]	Airbus	$0.0001\,^{\mathrm{deg}}/\sqrt{\mathrm{h}}$	$0.0005\,^{\mathrm{deg}}/\mathrm{h}$	Spacecraft

Table 1.1: Performance of some FOGs available on the market

1.5 Summary

The most important theoretical facts to keep in mind are these:

- The operating principle of FOG is the Sagnac effect: an interference of counterpropagating waves enclosing an area due to optical path length change caused by rotation.
- $\phi_S = \frac{8\pi^2 r^2 N\Omega}{c\lambda_0}$
- The output power of a Sagnac interferometer in full fiber optic implementation carries squared cosine dependence on ϕ_S.
- A practical FOG requires phase modulation, which increases sensitivity and allows sense of rotation determination.
- Parasitic phase shift causes sensor drift:
  - Polarization effects (Faraday effect, random birefringence and polarization mode coupling) can be reduced by PM fiber.
  - Nonreciprocities stemming from Kerr effect can be reduced by using broadband light source. EDFA based light source in particular.
  - Shupe effect – nonreciprocity stemming from stress and temperature time-gradients – can be reduced by mechanical stabilization and quadrupolar wind.

Part 2

Design

2.1 Elementary configuration

The first pass design, depicted in figure 2.1, was set up in the basic open-loop configuration as outlined in the previous section. The fiber spool is ca. 1 km long SMF-28 single-mode fiber simply wound around a 18 cm mandrel. The optical signal, coming from an SLED source, is modulated by an optoelectric modulator[1] and detected by an InGaAs PIN diode detector. The electrical output is further amplified by two 30 dB LF amplifiers, and the higher harmonics are filtered out. The demodulation is done by a lock-in amplifier based demodulator and the output logged.

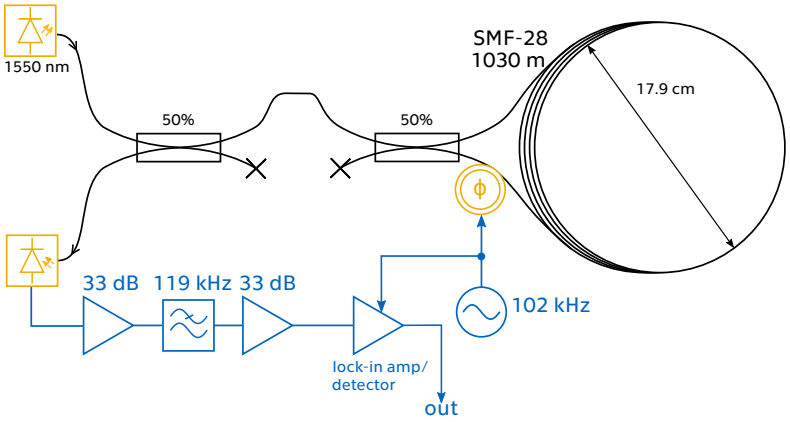

Figure 2.1: FOG setup

2.1.1 Equipment

The configuration utilizes following equipment:

[1] Marked Φ in the scheme.

- SMF-28 fiber: 998 m[2], $n = 1,468$ @ 1550 nm, NA = 0.14, wound in a ⌀ 17.9 cm coil (mean diameter, simple wind [3])
- PLC Splitters 1×2: symmetric, 1260 – 1650 nm, PM fiber, 4 dB max insertion loss (SQS Vláknová optika)
- Fiber coupled (SMF-28) InGaAs PIN diode detector: 1000 – 1650 nm, ~0.90 A/W (DPIN-23133, Precision Micro-Optics)
- 10G telecom optoelectric phase modulator: 1525 – 1605 nm, ~4.5 V drive voltage (Mach-10, Covega)
- Custom amplifiers: 33.4 dB @ 102 kHz (see Fig. A.7 in the appendix, p. 58, for frequency response)
- Custom low pass filter: c/o 119 kHz (see Fig. A.8 in the appendix, p. 59, for frequency response)
- Lock-in amplifier based demodulator: based on AD630ARZ chip (Analog Devices)
- SLED based fiber light source: Safibra OFLS-6, 1550 nm, 1.4 mW

2.1.2 Power budget

The setup was measured for insertion losses, to get an idea about measured powers. Uncertainties in logarithmic units were calculated according after [15].

- Source: 1.46 dBm
- Couplers: (1.00 ± 0.10) dB
- Modulator: (3.36 ± 0.21) dB
- Spool: 1.27 dB
- Total path loss[4]: (14.64 ± 0.45) dB

[2] Measured by an time-domain reflectometer. Full OTDR report is in the appendix, Fig. A.14, p. 63.
[3] Not quadrupolar or dipolar wind, which should reduce drift caused by Shupe effect
[4] Including discarded power (6 dB)

2.1.3 Output

We measured several outputs – always three times under these conditions: still, CCW rotating, CW rotating.

- No modulation
  - DC output
- 102.198 kHz sine modulated
  - Time domain
  - Spectra
  - Demodulated output

All raw data are presented in the appendix (Sec. A.1, p. 55). Selected results can be found in the following sections.

2.1.3.1 No modulation

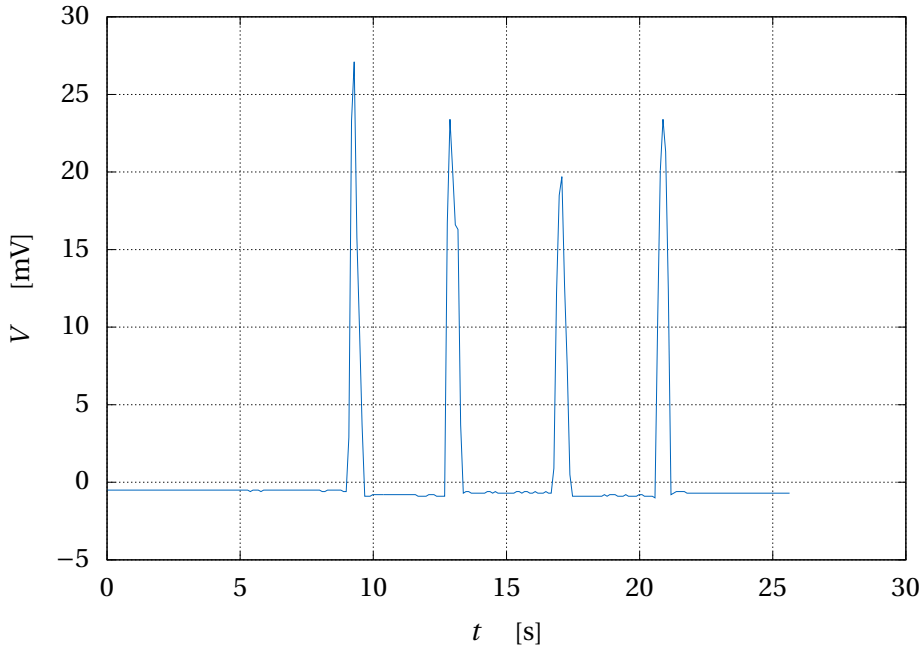

Figure 2.2: No modulation – DC output

Without any modulation, we can directly measure the Sagnac phase shift as DC output. This is the simplest measurement technique but useful only for demonstration purposes.

Firstly, it is not possible to distinguish the sense of rotation. The four peaks in Fig. 2.2 on the preceding page represent alternate CCW and CW rotations. Secondly, the sensitivity is the lowest possible and the output is strongly nonlinear. Both hindrances arise simply from the nature of the output function $\cos^2\left(\frac{\phi_S}{2}\right)$. The function is even, therefore the output is the same regardless of the sense of rotation, and the slope of the function, hence sensitivity, is exactly 0 when the gyro is still.

2.1.3.2 Phase modulation

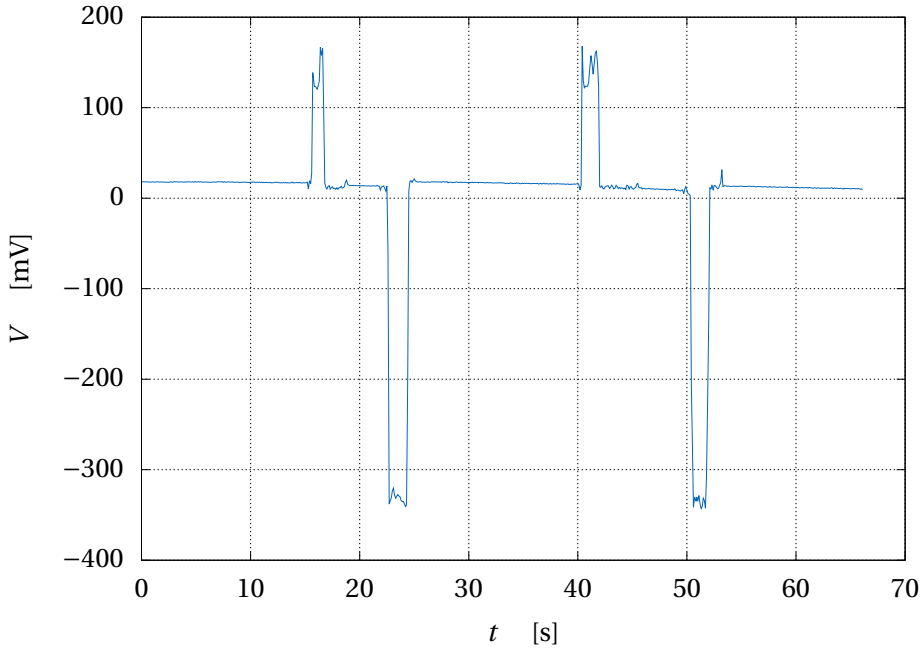

Figure 2.3: Demodulated output

As explained in the previous sections, applying phase modulation to the optical signal essentially biases the sensor so that the sensitivity (slope) is maximized while still, and the output function is odd.

The modulation frequency 102 kHz was devised to apply the optimal phase bias of 90° according to Ruffin [3]: $f_\lambda = \frac{c}{2nL}$, where L is the total Sagnac loop fiber length.

The difference between output under CCW and CW rotation of sine modulated gyro in the time domain (see figures A.2 and A.3 in the appendix, p. 56) shows that the opposing rotations are phase shifted by 180°. This conveniently translates to the polarity of the demodulated LF signal

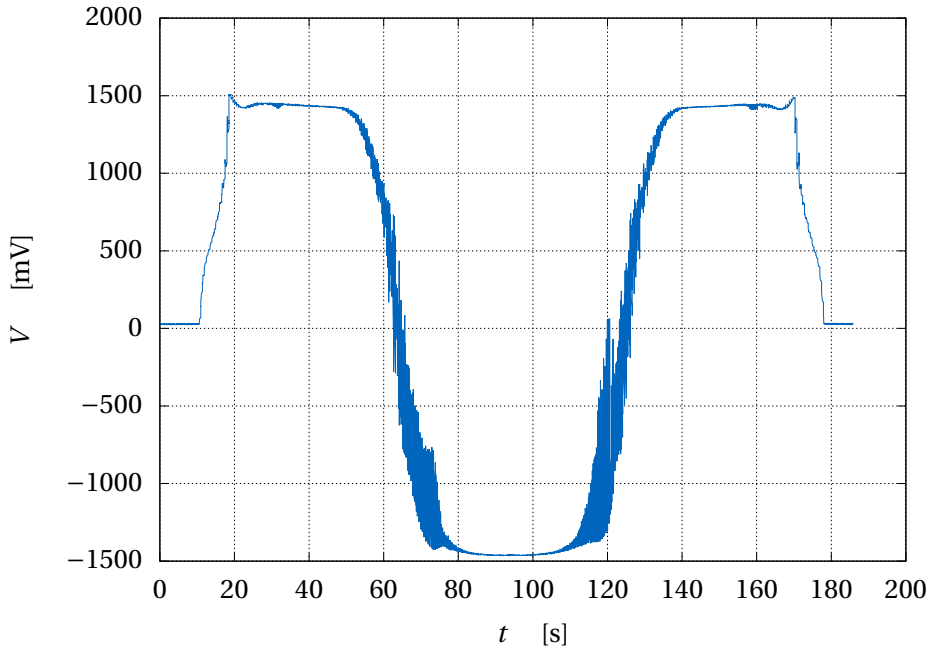

Figure 2.4: Gyro dynamic range

as can be seen in figure 2.3 on the preceding page.

The output in the frequency domain (see figures A.4, A.5, and A.6 in the appendix, p. 57 – 58) shows several frequency components of the detected (ie. electric) signal. These result from the phase modulation and can be derived via Bessel series (as explained before). The first even harmonic has the same frequency as the modulating signal (102 kHz). Other harmonics are present and are stronger than the further detected 102 kHz signal while still. The first harmonic gets significantly stronger under rotation.

2.1.4 Dynamic range

As explained before (Sec. 1.2.3) the gyro should have limited dynamic range due to the output's periodic nature. The gyro was spun up with a constant acceleration of 0.4 $^{\text{rpm}}/_{\text{s}}$ up to 20 rpm and then spun down with the same acceleration. The output is plotted on Fig. 2.4. The output voltage peaks at about 5 rpm, which means the open-loop configuration is very limited in its dynamic range.

2.2 Modulation setting

2.2.1 Model

Preliminary measurements showed that the output sensitivity of the Gyro varies wildly with modulation frequency. This is likely because the simplified model (Eq. 1.29 on page 22) is valid only if the gyro is perfectly biased (i.e. running at its eigenfrequency). It doesn't account for the phase shift that arises if the counterpropagating waves encounter the modulator at different time while still.

Therefore we made a mathematical model based on Sagnac effect relations derived above (Sec. 1.1.2 on page 17) that would give us ideal frequency dependencies of modulation frequency and index. These should help us interpret the experimental results and devise a method to properly set up the modulation frequency and index.

The derivation involves very cumbersome algebra, because of that, it is presented in the appendix (p. 65). The resulting relation is:

$$P_{out} = \frac{1}{4}\cos^2\left|\frac{4cL\pi r\Omega + h\lambda_0(\sin(t\omega_m))(c^2-r^2\Omega^2) - h\lambda_0(c^2-r^2\Omega^2)\left(\sin\left(\omega_m\left(t+\frac{L(cn-r\Omega)}{c^2-r^2\Omega^2}\right)\right)\right)}{2\lambda_0(c^2-r^2\Omega^2)}\right| P_{in} \tag{2.1}$$

It was implemented in the Matlab computing environment. In essence, the script simulates the signal in time domain, computes its spectrum via fast Fourier transform and takes the spectral line of the modulation frequency as the output power.

2.2.2 Modulation frequency

From the signal processing point of view, the choice of modulation frequency doesn't matter as long as the demodulator can detect the particular frequency – the modulation frequency should not affect maximum detected signal amplitude. However it is very advisable to set the modulation frequency to spool's eigenfrequency ($f_\lambda = c/2nL$ see Sec. 1.2.3) to avoid parasitic errors due to defects of the modulation [6].

According to both simulation and measurement, the output power is actually very much dependent on modulation frequency. The measured data[5] are presented in Fig. 2.5 on the facing page, computed results in Fig. A.3.1 on page 60 in the appendix. In both cases sinewave modulation was applied.

According to the numerical model the output power is either at a local minimum or maximum when the gyro is running at its eigenfrequency (99.204 kHz in the simulation). However, the dependency has many local

[5] The bandpass filter was removed, to make the measurement possible.

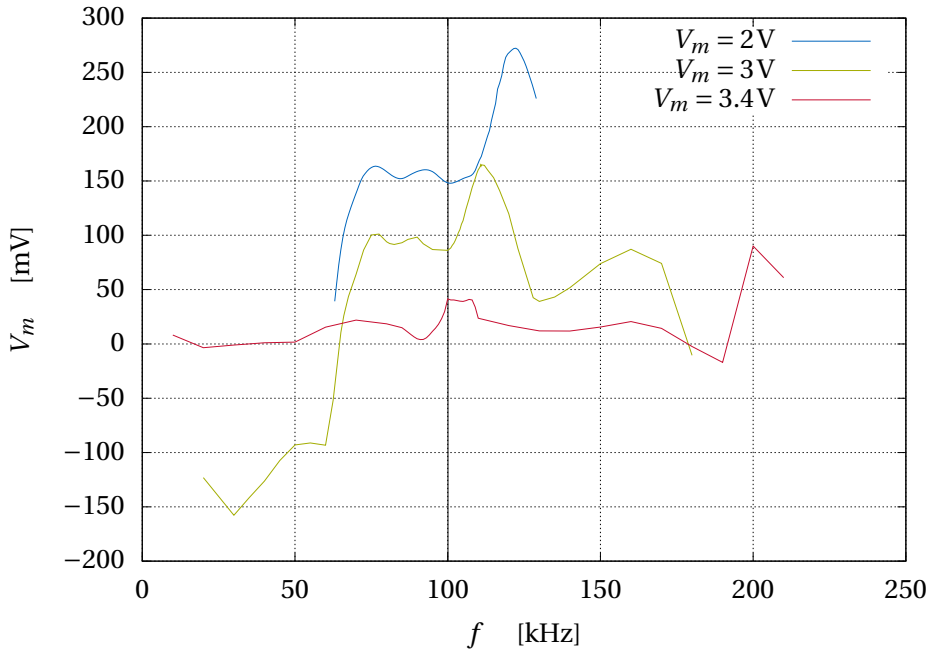

Figure 2.5: Modulation – measured frequency dependence

maxima and minima at its harmonics. Measured data show very wild frequency dependency, although the general shape, major peaks and drops at the harmonics seem to be the same.

To measure the eigenfrequency we need to find the local extreme. Devised method goes as follows:

1. Estimate the eigenfrequency of the gyro.
2. Set the modulation voltage arbitrarily, but make sure the output isn't noisy and the demodulator does give measurable output at the estimated eigenfrequency under slow rotation.
3. Spin the gyro at constant low revolution speed[6].
4. Measure the output voltage as a function of modulation frequency.
5. Find a local minimum or maximum near the estimated eigenfreuency.
6. Repeat for several modulation indices and revolutions to verify the value, because there are other extremes near f_λ, and the extreme sought may not be very pronounced.

[6]Shouldn't be much above detection threshold as the gyro could be in its nonlinear region

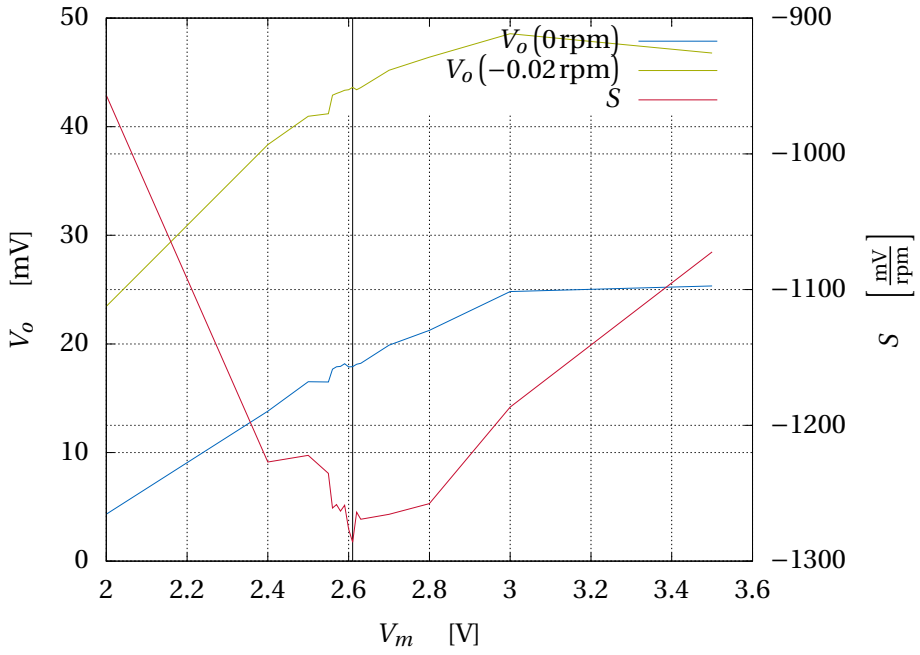

Figure 2.6: Modulation – measured modulation voltage dependece.

The eigenfrequency of our gyroscope was determined to be **100.1 kHz** – a fairly close value to the theoretical value of 102 kHz determined from spool's length and refractive index.

2.2.3 Modulation index

The optimal modulation index of 1.841 (see Sec. 1.2.3) is an abstract value dependent on the response of a particular phase modulator, which is rarely known. Therefore an experimental method to set up the modulation voltage is needed even more so. Additionally, both numerical model and actual measurements show that the optimal modulation index is frequency dependent as well.

We need to measure the sensitivity at various modulation voltages. This can be done by measuring output while still and under low rotational speed and calculating slope $\left(S = \frac{V_1 - V_0}{\Omega}\right)$. Simulated results are presented in Fig. A.3.2 on page 62 in the appendix. The method is fairly simple:

1. Set the modulation to eigenfrequency.
2. Set up the modulation voltage.
3. Measure the output voltage a still gyro.

4. Measure the output voltage of the gyro under chosen low rotation rate.[7]
5. Repeat 2 – 4 until whole voltage dependecy is obtained
6. Calculate slope, plot, and find the global minimum[8].

The measured data are in plotted on Fig. 2.6 on the preceding page – the red plot is the sensitivity (the right y axis). Output below modulation voltage of 1.5 V was burdened by heavy modulator noise (standard deviations close in value to measured output values). First sensitivity peak (negative) was located at **2.61 V**. We weren't able to detect any further peaks, because they are above modulator's voltage rating of 4.5 V.

2.3 Stability and noise assessment

To evaluate gyroscope's performance, we need a way to measure its drift and noise performance. Conveniently enough, Allan's variance (usually used to measure oscillator frequency stability) can be used to quantify both.

Should the output of a sensor be measured over long period, its Allan variance, a function of observation period τ, as an estimator in "frequency domain"[9] is defined [16, 17]:

$$\sigma_y^2(\tau, N) = \frac{1}{2(N-1)} \sum_{i=0}^{N-2} \left(\bar{y}_{i+1} - \bar{y}_i\right)^2 \tag{2.2}$$

N	Number of samples
τ_0	Sampling period
$\bar{y}$	Sample value

In principle, the measured data of N samples is divided into N/n blocks of even length, and the values within the blocks are averaged out. Squared deviations of neighboring blocks are averaged out. This is done for n spanning from 1 close to N. Product of n and the sampling period gives the observation period $\tau = n \cdot \tau_0$.

However, if the averaging process includes preceding blocks as well, the result accuracy is improved [16].Estimator with overlapped τ is

$$\sigma_y^2(n\tau_0, N) = \frac{1}{2n^2(N-2n+1)} \sum_{j=0}^{N-2n} \left(\sum_{i=j}^{j+n-1} \bar{y}_{i+n} - \bar{y}_i \right)^2 \tag{2.3}$$

[7] Same restriction as with frequency measurement applies: the rotational speed shouldn't be much above detection threshold.

[8] Minimum if adhering to the right-hand rule. Otherwise, it's a maximum

[9] Original Allan variation is defined either over phase domain or frequency domain. This applies to oscillator measurement. In gyroscope measurement the same mathematical abstraction translates to angular velocity domain (originally phase) and angle domain (frequency).

The square root of Allan variation is Allan deviation which can be used for performance assessment.

Two figures read from Allan's deviation are important [7, 18]. *Angle random walk* coefficient is a measure of white-noise-like terms in the gyro's output[7, 17]. It is defined[17]

$$\sigma(\tau) = \frac{N}{\sqrt{\tau}}, \tag{2.4}$$

N is the coefficient, hence its dimension is $\mathrm{U}\sqrt{\mathrm{s}}$, where U is the measured unit.[10]

Bias instability[17] is a measure of sensor drift. It is defined[17]

$$\sigma(\tau) = \sqrt{\frac{2\ln 2}{\pi}} B \tag{2.5}$$

B is the coefficient, hence its dimension is the same as the measured unit.

In addition, the minimal value of the Allan deviation plot is the lowest possibly detectable rotation rate [7, 18].

To acquire the N and B, the Allan variance needs to be fitted with following model [17] via least squares:

$$\sigma^2(\tau) = \frac{R^2\tau^2}{2} + \frac{K^2\tau}{3} + B^2\left(\frac{2}{\pi}\right)\ln(2) + \frac{N^2}{\tau} + \frac{3Q^2}{\tau^2} \tag{2.6}$$

Allan variance with overlapped τ was implemented via *Allantools*[11] library in Python. Least squares fitting was done in Mathematica.

2.3.1 SM-SLED setup stability

The basic setup was measured for about 11 hours for stability. Its Allan deviation plot is in Fig. 2.7 on the facing page. Resulting parameters are

- $N = 3.65\,\mu\mathrm{V}\sqrt{\mathrm{s}}$
- $B = 2.74\,\mu\mathrm{V}$
- $\Delta V = 0.234\,\mathrm{mV}$

As it can be seen on the plot, the minimal detectable rate is particularly bad due to a bump in the plot. The source of this unexpected bump from ca. $\tau = 2\,\mathrm{s}$ to $\tau = 20\,\mathrm{s}$ seems to be drift rate ramp R [17]. It can be acquired from the Allan variation in the same way as random walk and bias instability and the value is

$$R = 1.41\,\mathrm{mV/s},$$

[10] $\frac{\mathrm{rad}}{\mathrm{s}}$ or other rotation rate units. Alternately V in case of direct output

[11] https://pypi.python.org/pypi/AllanTools

which is three orders of magnitude stronger than N and B.

The rate ramp is a deterministic error, unlike the other coefficients, and it indicates source instability [17].

This, sadly, makes the gyroscope very unstable. Even on 10 second scale, drift is more apparent than noise. Because of that further improvements are needed.

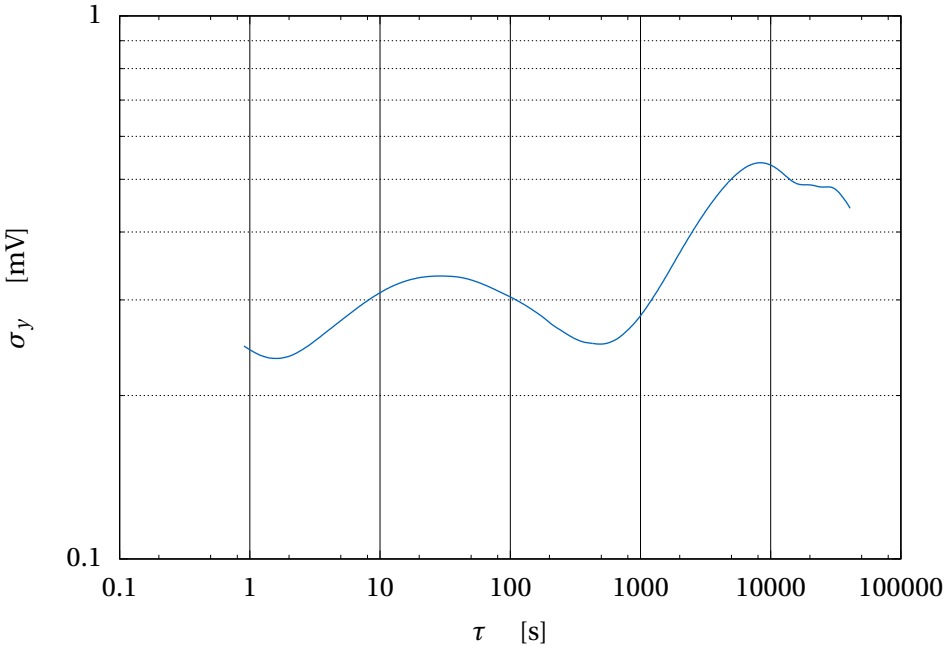

Figure 2.7: SMF spool, SLED source – Allan deviation

2.4 Erbium-doped-fiber light source

An SLED light source is incoherent enough to eliminate Kerr induced drift and polarization mode coupling. However, the power coupled to a single mode fiber is limited, because of fiber's narrow acceptance cone and limited power output of the SLEDs [9]. To increase the sensitivity (or scale factor) of the gyro, a fairly high power source is required. Higher optical powers reduce the noise increase the sensitivity after Eq. 1.24 on page 21. A laser not being an option due to Kerr effect, polarization mode coupling and backscattering, erbium-doped fiber superluminescent source seems to be the key.

A light source based on EDFA was devised. The actualy gyroscope can be seen in Fig. 2.8 on the following page. The Er-doped fiber is pumped

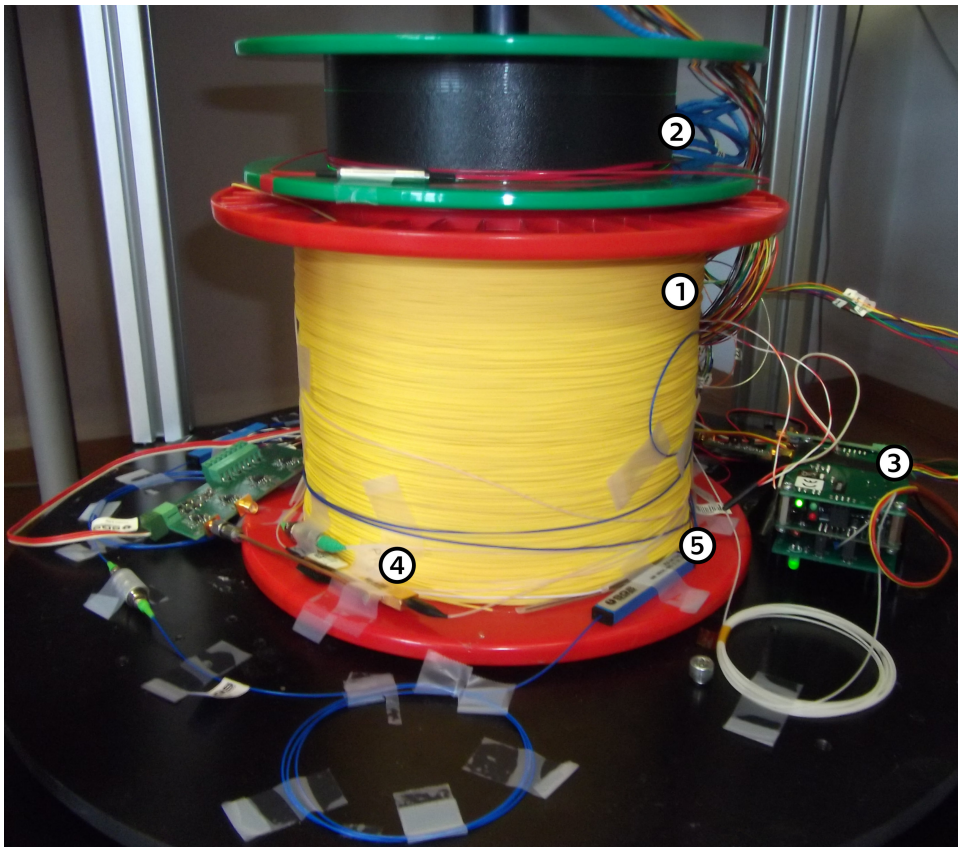

Figure 2.8: The prototype gyro on a turntable
1 – Single mode spool, 2 – Er-doped fiber, 3 – Laser pump, 4 – Phase modulator, 5 – Fiber coupler

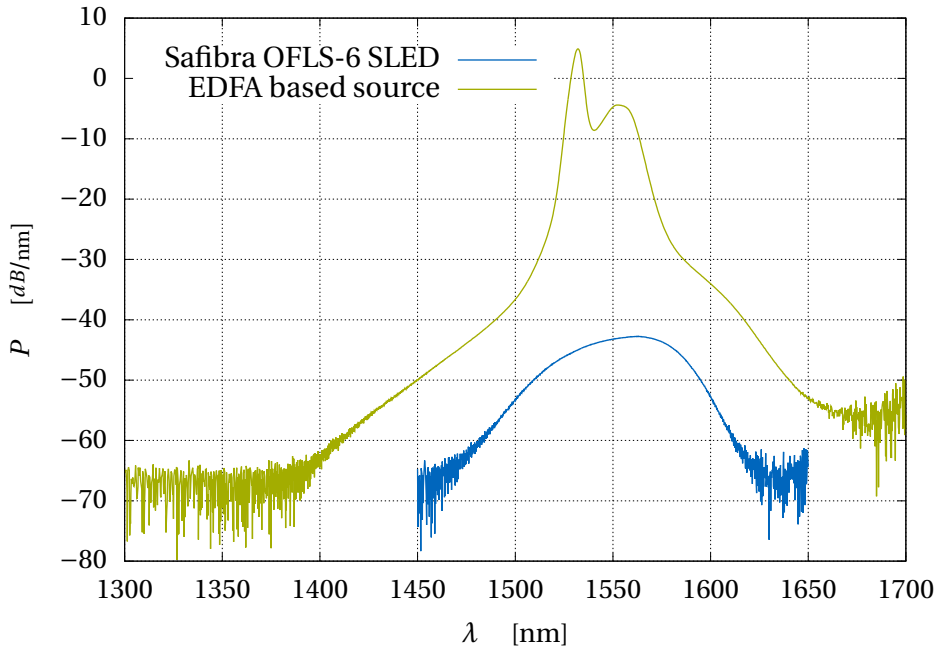

Figure 2.9: Source spectra

by a 975.6 nm, 0.5 W laser. The spectrum of the light source compared to the SLED source can be seen in Fig. 2.9. The 1530 and 1560 nm peaks are typical of erbium emission spectrum [9], and there's still room for improving the bandwidth and spectrum flatness. 10 dB bandwidth of the EDF source is 31 nm, the bandwidth of the SLED is 97 nm. Chang et al. [19] suggest pumping the Er-fiber from both directions via a WDM coupler, which should filter out the uncanny peaks. Such configuration should offer excellent bandwidth and spectral flatness.[12]

After all, the EDF source offers much more output power: 15.1 dBm compared to 1.5 dBm of the SLED. This should translate to steeper scale factor of the gyro, with sensor drift remaining at comparable levels.

2.4.1 Sensor response

Being acceptably stable, the open-loop setup with EDF source was measured for its sensor response or scale factor. The gyro was measured on a turntable driven by an asynchronous motor with feedback control. This means the rotation control and precision aren't perfect. The results are,

[12] Chang et al.'s setup: 22 nm 3 dB bandwidth, 0.2 dB spectral flatness, 5 mW output power

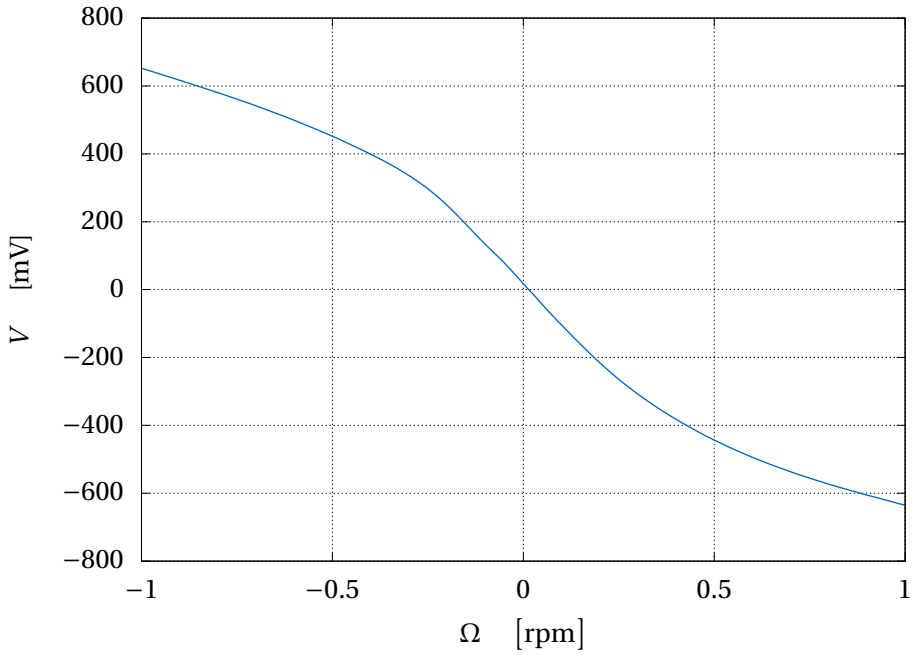

Figure 2.10: SM setup response – high rotation rate

however, fairly satisfactory.

The nonlinear nature of the open-loop gyro can be seen on Figure 2.10. Without additional signal processing the sensor can be used within its linear region, this means up to ca. 0.2 RPM. This is adequate for precision measurements of minor rotation rates, not for inertial navigation systems. The digital closed-loop configuration should greatly enhance the dynamic range (see Sec. 1.4).

Analyzing the response for minor rotation rates (see Fig. 2.11), we can calculate the scale factor of the gyroscope. A transfer function was obtained by taking the least-squares linear regression of minor rotation rate readouts from -0.01 to 0.01 rpm (including standard deviations due to multiple measurements):

$$V = [(-1221.9 \pm 9.9)\,\Omega/\mathrm{rpm} + (17.72 \pm 0.22)]\,\mathrm{mV}$$

Hence its scale factor is

$$S = 7.38\,^{\mathrm{deg/s}}/_{\mathrm{V}}$$

.

Taking the root-mean-squared error of the residuals we obtain the average deviation of the rotation rate from the ideal function, which can be

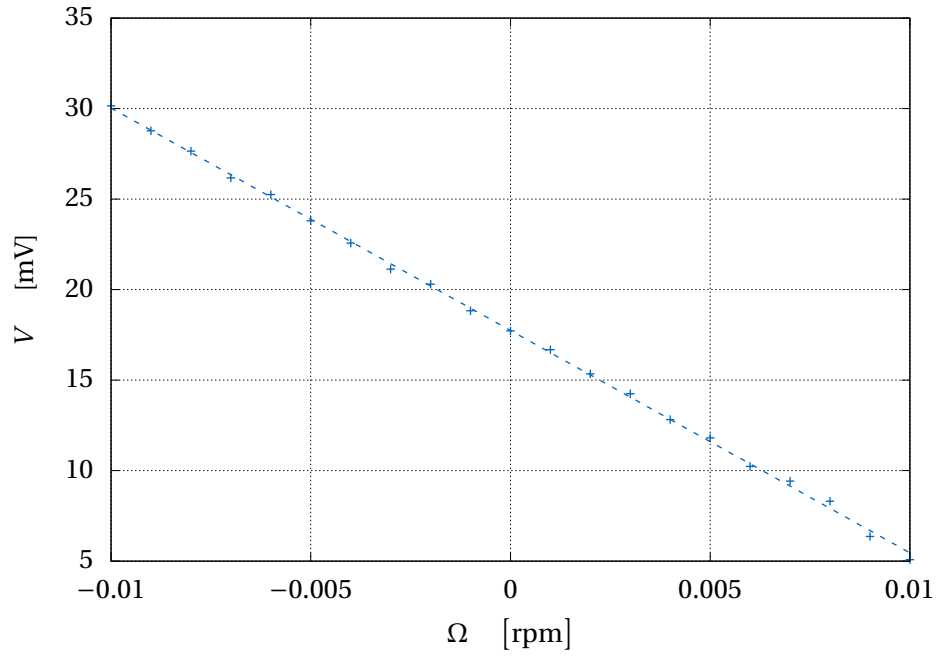

Figure 2.11: SM setup response – minor rotation

used to asses the lowest detectable rate of the sensor:

$$\mathrm{MSE} = 0.093\,\mathrm{mV}^2, \quad \Delta\Omega = 0.36\,^{\mathrm{deg}}/_{\mathrm{h}}$$

. $0.36\,^{\mathrm{deg}}/_{\mathrm{h}}$ is actually better than Earth's rotation speed of $15\,^{\mathrm{deg}}/_{\mathrm{h}}$. But we can't quickly jump into conclusions, because the output voltage was averaged out of 100 values over the period of about four seconds[13] and is likely subject to sensor drift. More robust assessment of accuracy should be done through Allan's variance.

2.4.2 Sensor stability

The EDF-source setup was left running over a weekend and the output logged. The Allan curve is plotted in Fig. 2.12. Unlike the setup with an SLED source, it shows a typical curve expected from an FOG. The random walk, bias instability and lowest detectable rate values are these:

$$N = 5.18\,^{\mathrm{deg}}/\sqrt{\mathrm{h}}, \quad B = 1.37\,^{\mathrm{deg}}/_{\mathrm{h}}, \quad \Delta\Omega = 0.70\,^{\mathrm{deg}}/_{\mathrm{h}}$$

[13] Varying, depending on multimeter's output

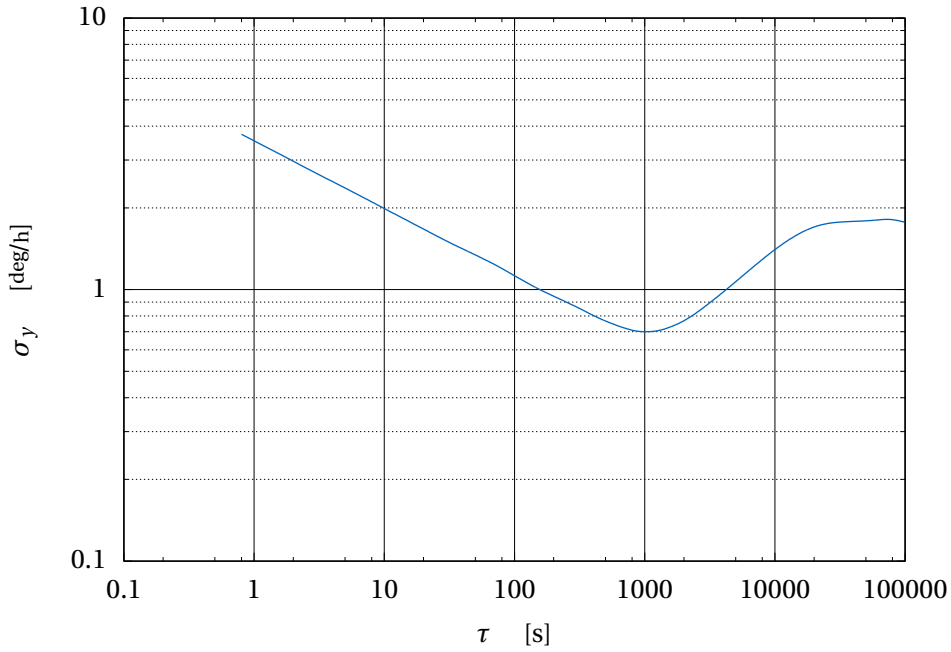

Figure 2.12: SM spool, EDF source – Allan deviation

While the results aren't exactly stellar[14], we got entirely rid of the unsightly bump caused by rate ramp (compare with Fig. 2.7). Since any previously analyzed drift sources should be either unaffected or worse with choosing a more powerful EDF source over an SLED, we may confirm that it was caused by the instability of the light source.

The bias instability is quite comparable to commercial low-grade gyros (see Tab. 1.1 on page 26). However, the random walk seems to be very unsatisfying, therefore additional work is needed to reduce the noise.

Additionally, all the figures is lower than Earth's rotation rate (15 deg/h). This means, with long enough integration time to eliminate white noise, the gyro should be capable of detecting Earth's revolution. This is consistent with the minimal detectable angular velocity calculated through mean squared error during sensor response measurement (0.36 deg/h, averaging time about four seconds), although it overestimated the performance twice when compared to lowest detectable rate calculated via Allan's variation ($\Delta\Omega = 0.70$ deg/h).

[14] About 3 orders of magnitude worse than a state-of-the-art space-grade navigation FOG Astrix 200 by Airbus[14].

2.5 Polarization-maintaining fiber configuration

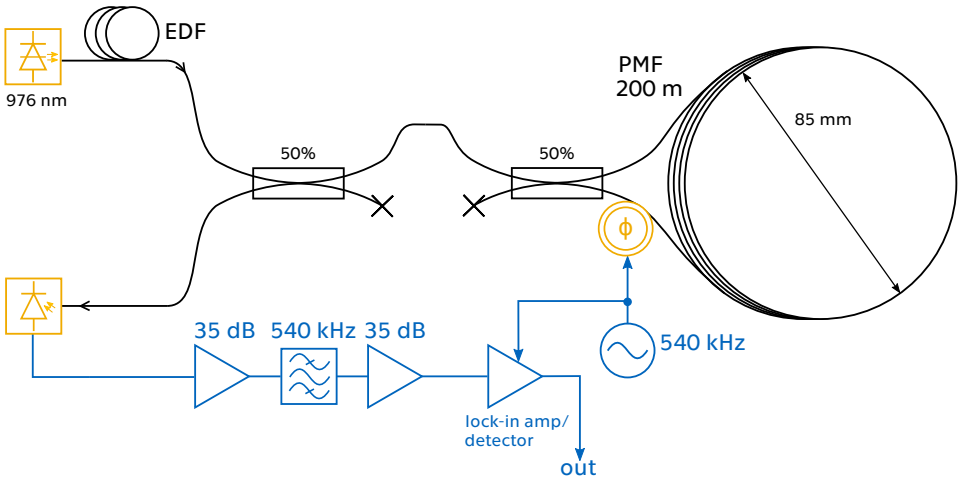

Figure 2.13: PM fiber configuration

2.5.1 Preface

Unfortunately, due to unforeseen circumstances, the connectors of the PM spool tore off during the stability measurement. PM fiber welding is a rather intricate process, and the FEE doesn't possess the equipment needed to do so. Therefore we can't compare the stability of SM and PM spool as it is asked in the assignment.

2.5.2 Setup

This configuration expands upon previous setups. The 1 km long SM fiber spool was replaced by a shorter polarization maintaining fiber spool quadrupolary wound. The wind should reduce instabilities induced by the Shupe effect (Sec. 1.3.3). Defined birefringence of the PM fiber should reduce any undesirable polarization effects (Sec. 1.3.1). The shorter length entails that gyro's sensitivity or scale factor will, of course, be lower. Furthermore, the electronics need to accommodate a higher eigenfrequency according to the aforementioned formula $f_\lambda = \frac{c}{2nL}$.

The new spool is 200 m long and 85 mm in diameter. The new electronic filter is 510 kHz bandpass. Otherwise, the components are the same as in the single-mode EDF setup.

2.5.3 Response

The PM setup was measured for its rotation response in the same way as the SMF pass. (see section 2.4.1)

The high rotation rate response (see Fig, A.15) shows that the linear region of the sensor spans up to 1.2 rpm.

The low rotation rate response (see Fig. 2.14) was used to calculate transfer function of the gyro and its general accuracy:

$$V = (-711.91\Omega/\text{rpm} - 1.41)\ \text{mV}$$

$$S = 4.27\,^{\text{deg/s}}/\text{V}$$

$$\text{MSE} = 0.081\,\text{mV}^2, \quad \Delta\Omega = 0.58\,^{\text{deg}}/\text{h}$$

$0.58\,^{\text{deg}}/\text{h}$ is almost twice as worse as calculated $\Delta\Omega = 0.36\,^{\text{deg}}/\text{h}$ of the SM spool setup. This is certainly caused by the shorter fiber and lower spool radius. However, even in this case we can't quickly jump into conclusions – proper assessment should be done through long term measurement of noise and stability, which is, sadly, impossible at the moment of submitting this work. Although, we may cautiously propose that its noise performance is better – even though its sensitivity should be about 11 times worse than the SM spool according to $\phi_S = \frac{4\pi r L \Omega}{c\lambda_0}$, the calculated lowest detectable rate via MSE is only twice as worse.

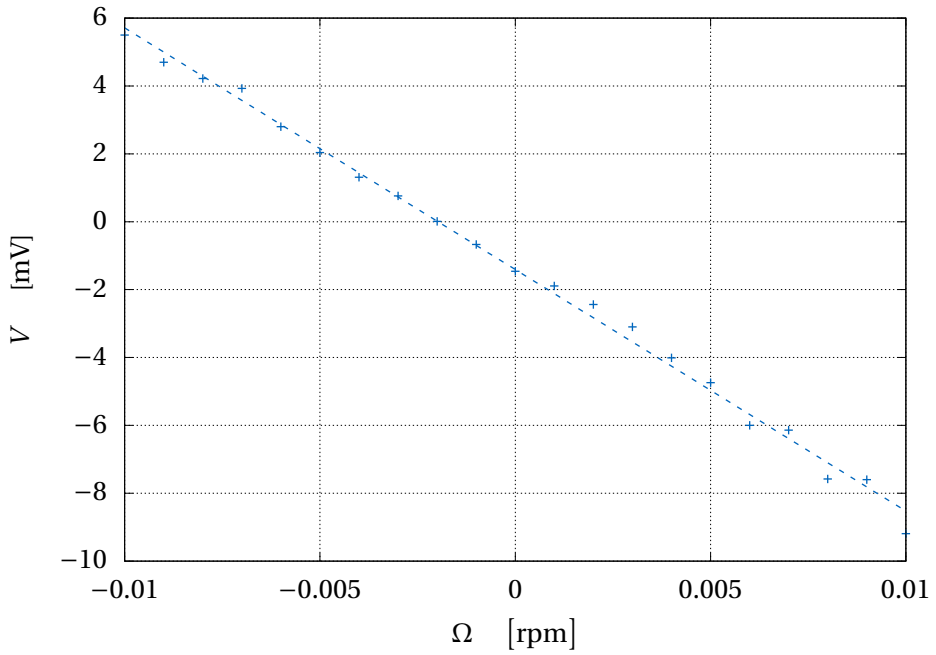

Figure 2.14: PM setup response – minor rotation

2.6 Summary

We shall sum up the experimental results.

- Basic open-loop configuration demonstrated rudimentary functionality.
- Any open-loop configuration has inherently limited dynamic range.
- SMF – SLED configuration shows very significant drift due to rate random walk.
- A method to setup the gyro modulation was devised.
- Gyro's eigenfrequency in the SMF configuration is 100.1 kHz, optimal modulation voltage 2.61 V.
- SMF – EDF source configuration has random walk of $RW = 5.18\,^{\mathrm{deg}}/\sqrt{\mathrm{h}}$, bias instability of $B = 1.37\,^{\mathrm{deg}}/\mathrm{h}$, lowest detectable rate of $0.70\,^{\circ}/\mathrm{h}$, and Scale factor of $7.38\,^{\mathrm{deg/s}}/\mathrm{V}$.
- PMF – EDF source configuration will likely show better noise and drift performance, but proper determination was impossible due to rapid unplanned disassembly.

Part 3

Conclusion

We set up a fiber-optic gyroscope in an open-loop configuration with a single-mode fiber spool and Er-doped fiber light source.

An SLED based light-source showed unsatisfying stability performance. The SLED source was replaced with EDFA based one, which eliminated rate ramp and allowed for meaningful readouts.

The phase modulation of the gyro is a necessity to make the rotation response linear, albeit within a limited dynamic range, and maximize the sensitivity. We devised a simple method to properly set up the modulation frequency and modulation voltage directly from the output voltage. The frequency and voltage for the 998 m spool and our particular modulator are 100.1 kHz and 2.61 V.

From there on we measured the scale factor of the gyroscope which is $7.38\,^{\mathrm{deg/s}}/\mathrm{V}$.

We assessed noise and stability performance based on Allan's variance, which can be calculated from a long term measurement. Random walk of the gyro, which quantifies noise performance, is $5.18\,^{\mathrm{deg}}/\sqrt{\mathrm{h}}$. Bias instability, which quantifies drift performance is $BI = 1.37\,^{\mathrm{deg/h}}$. Lowest possible detectable rate is $\Delta\Omega = 0.70\,^{\mathrm{deg/h}}$ This means that with long enough integration time the gyro should be capable of detecting Earth's rotation speed of $15\,^{\mathrm{deg/h}}$, although these figures are still far from state of the art FOGs and worse than commercial FOGs, although bias instability seems comparable to low-grade FOGs. The random walk is, on the other hand, poor.

Some measurements were done with an advanced polarization maintaining fiber spool, which should significantly reduce drift caused by thermal gradients and polarization effects. However, during a stability measurement, the connectors of the spool tore off and we were unable to compare its noise & stability performance with the single-mode spool.

The gyroscope has a very limited dynamic range of approximately -0.2 to 0.2 rpm. In the future, the range could be improved by implementing a digital closed-loop configuration, which is done entirely on the electronic

signal processing and modulation part. The closed-loop configuration also makes the response entirely linear.

An experimental method devised by Chang et al.[19] could be used to flatten the EDF source spectrum and increase its bandwidth to potentially reduce Kerr effect induced drift even more.

The next step in the development of the gyroscope is reducing the noise – the PM spool could potentially achieve that. From there on two additional axes should be added for complete measurements in all spatial dimensions.

References

[1] H. J. Arditty and H. C. Lefèvre. Sagnac effect in fiber gyroscopes. *Optics Letters*, 6(8):401–403, August 1981.

[2] S. Merlo, M. Norgia, and S. Donati. Fiber Gyroscope Principles. In J. M. López-Higuera, editor, *Handbook of Optical Fiber Sensing Technology*, pages 331–348. John Wiley & Sons, 2002.

[3] P. B. Ruffin. Fiber Optic Gyroscope Sensors. In S. Yin, P. B. Ruffin, and F. T. S. Yu, editors, *Fiber Optic Sensors*, pages 334–364. Taylor & Francis, 2008.

[4] S. T. Thornton and A. Rex. *Modern Physics for Scientists and Engineers*. Brooks/Cole, 2013.

[5] R. Hui and M. O'Sullivan. *Fiber Optic Measurement Techniques*. Elsevier, 2009.

[6] H. C. Lefèvre. Fundamentals of the Interferometric Fiber-Optic Gyroscope. *Optical Review*, 4(1A):20–27, 1997.

[7] M. Digonnet. Fiber Optic Gyroscope. COST Summer School Madeira Island, September 2012.

[8] R. Boyd. *Nonlinear optics*. Academic press, 2003.

[9] G. P. Agrawal. *Fiber-Optic Communication Systems*. Wiley, 1997.

[10] KVH Industries Inc. DSP-3000 Fiber Optic Gyro. URL `http://www.kvh.com/Commercial-and-OEM/Gyros-and-Inertial-Systems-and-Compasses/Gyros-and-IMUs-and-INS.aspx`. [Online; accessed 22-May-2017].

[11] Saab AB. 8088 000-112 Fiber Optic Gyro. URL `http://saab.com/naval/weapon_systems/gyro-products/fiber-optic-gyro-products-naval/`. [Online; accessed 22-May-2017].

[12] EMCORE Corporation. EMP-1 Fiber Optic Gyroscope (FOG). URL http://emcore.com/product-category/fiber-optic-gyro-fog-components-sensors/fiber-optic-gyroscopes-fog-components/. [Online; accessed 22-May-2017].

[13] Al Cielo Inertial Solutions Ltd. FOG 53. URL http://www.alcielo.com/fiber-optic-gyros. [Online; accessed 22-May-2017].

[14] Airbus Group SE. Astrix® 200. URL https://spaceequipment.airbusdefenceandspace.com/avionics/fiber-optic-gyroscopes/astrix-200/. [Online; accessed 22-May-2017].

[15] C. F. M. Carobbi. The Use of Logarithmic Units in the Uncertainty Evaluations of EMC Measurements. URL https://www.researchgate.net/publication/241707708_The_Use_of_Logarithmic_Units_in_the_Uncertainty_Evaluations_of_EMC_Measurements. [Online; accessed 15-May-2017].

[16] IEEE Standard Definitions of Physical Quantities for Fundamental Frequency and Time Metrology - Random Instabilities. *IEEE Std 1139-1999*, 1999.

[17] IEEE Standard Specification Format Guide and Test Procedure for single-axis interferometric Fiber Optic Gyros. *IEEE Std 952-1997*, 1997.

[18] Freescale Semiconductor. Allan Variance: Noise Analysis for Gyroscopes, February 2015. URL http://cache.freescale.com/files/sensors/doc/app_note/AN5087.pdf. [Online; accessed 15-May-2017].

[19] J. L. Chang and M. Q. Tan. Experimental optimization of an erbium-doped super-fluorescent fiber source for fiber optic gyroscopes. *Journal of Semiconductors*, 32(10), October 2011.

List of Figures

Appendix A

Measured and simulated data

A.1 Sinewave modulation

A.1.1 Time domain

sin klid.png sin klid.bb

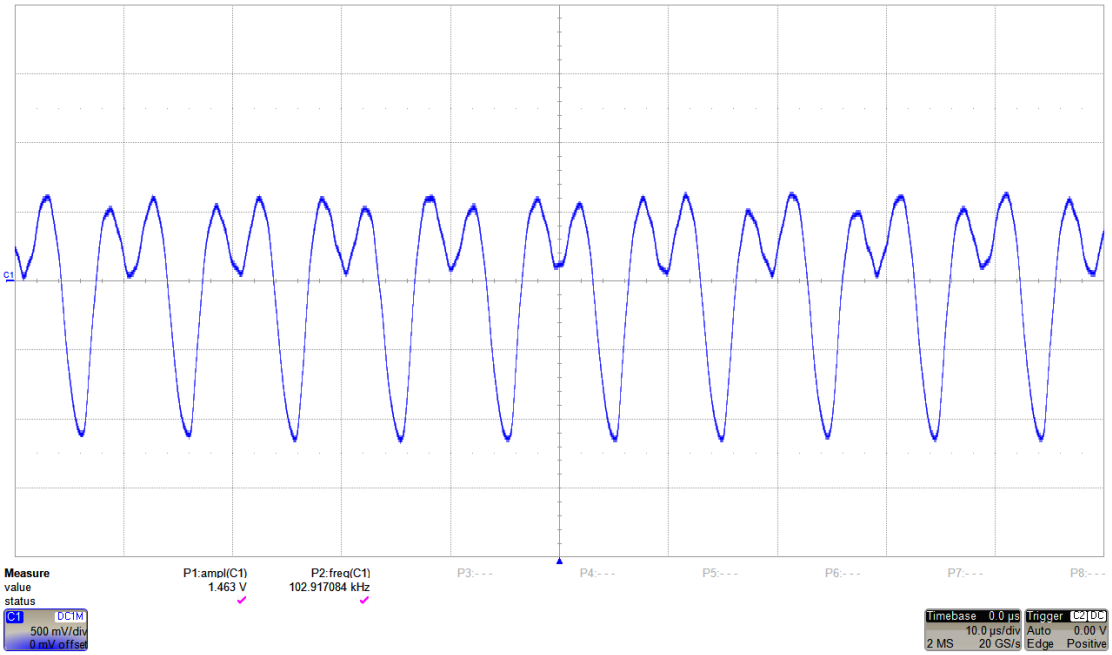

Figure A.1: Sinewave modulation – time domain – still gyro

sin ccw.png sin ccw.bb

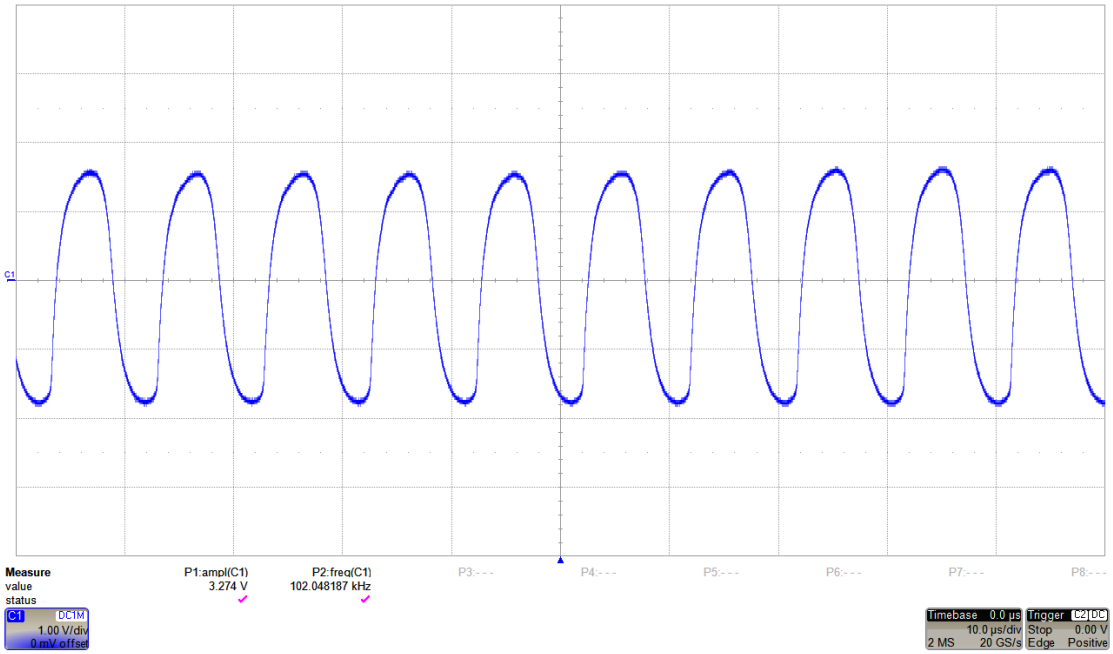

Figure A.2: Sinewave modulation – time domain – ccw rotation

sin cw.png sin cw.bb

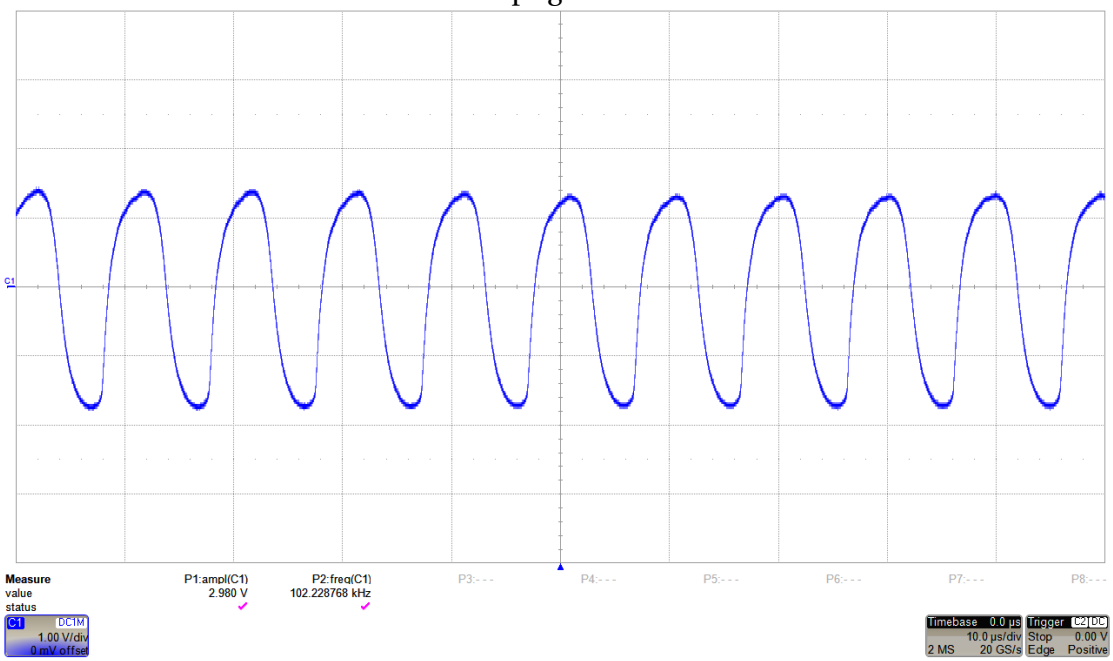

Figure A.3: Sinewave modulation – time domain – cw rotation

A.1.2 Frequency domain

klid.png klid.bb

Peaks	Frequency	Amplitude
1	204.40 kHz	14.7 dBm
2	408.79 kHz	-2.9 dBm
3	102.19 kHz	-4.3 dBm
4	306.60 kHz	-10.2 dBm
5	61.41 kHz	-21.3 dBm
6	30.66 kHz	-21.6 dBm
7	353.86 kHz	-22.7 dBm
8	92.65 kHz	-22.8 dBm
9	149.43 kHz	-23.1 dBm
10	54.93 kHz	-24.3 dBm

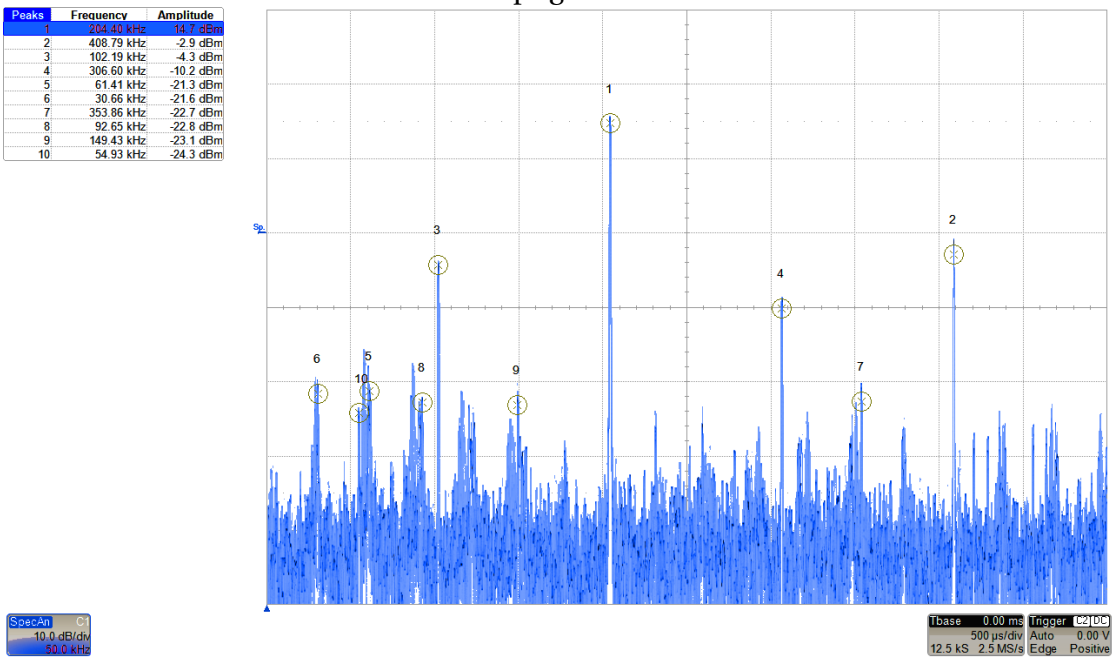

Figure A.4: Sinewave modulation – spectrum – still gyro

ccw.png ccw.bb

Peaks	Frequency	Amplitude
1	204.40 kHz	12.3 dBm
2	102.20 kHz	10.5 dBm
3	306.59 kHz	2.4 dBm
4	408.80 kHz	-14.1 dBm
5	57.50 kHz	-19.4 dBm
6	86.17 kHz	-21.2 dBm
7	28.82 kHz	-22.3 dBm
8	114.92 kHz	-24.1 dBm

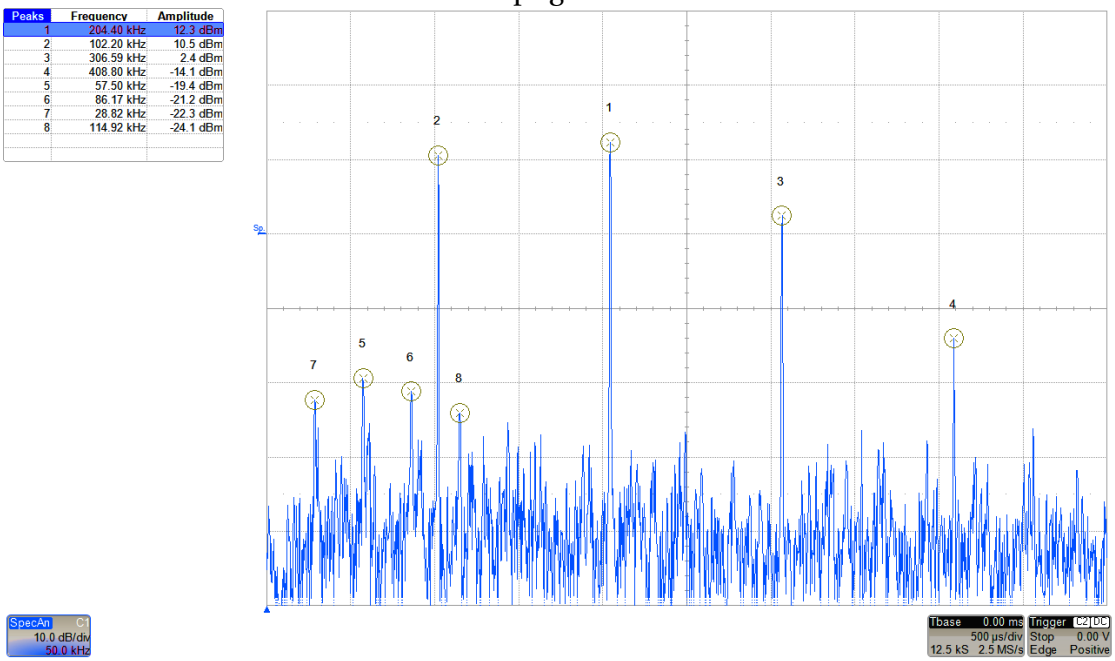

Figure A.5: Sinewave modulation – spectrum – ccw rotation

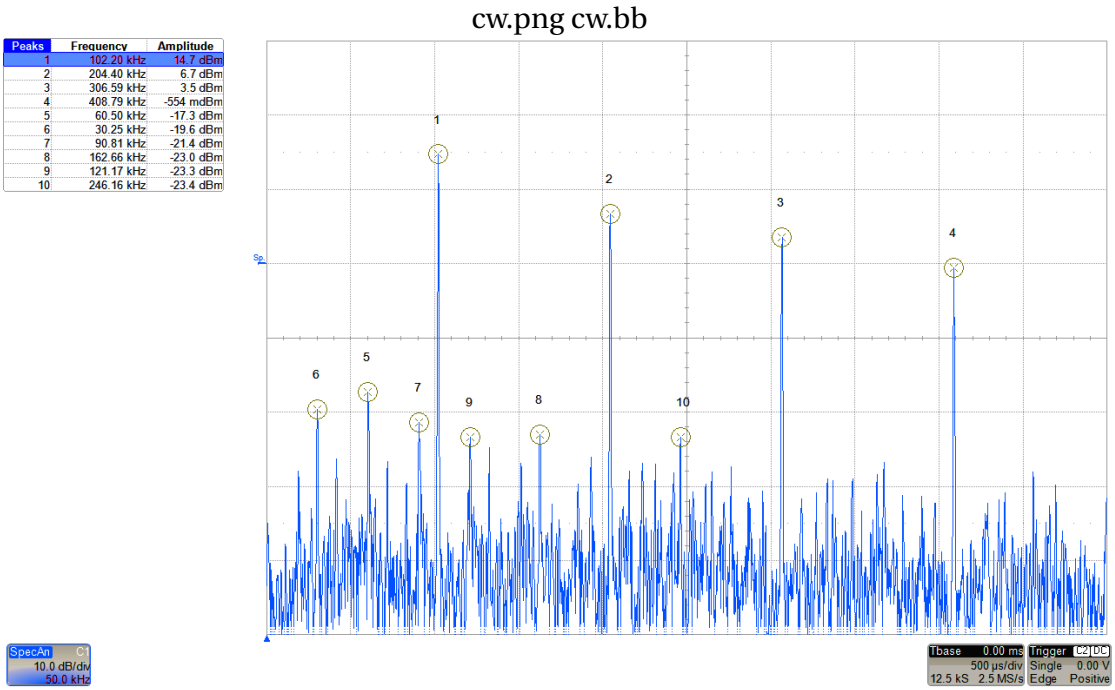

Figure A.6: Sinewave modulation – spectrum – cw rotation

A.2 Filter and amplifier frequency response

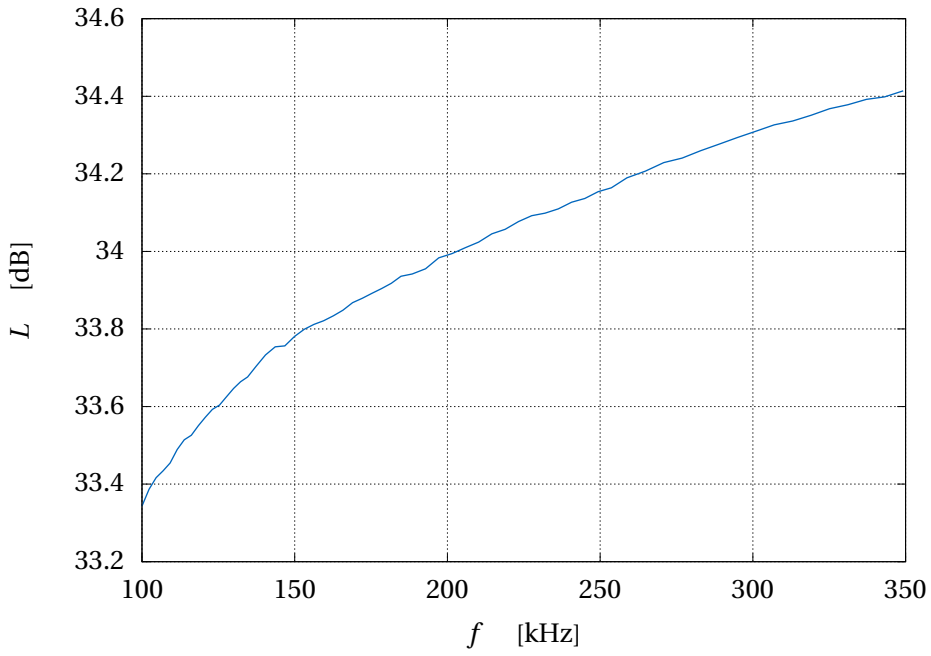

Figure A.7: Frequency response of the used amplifiers

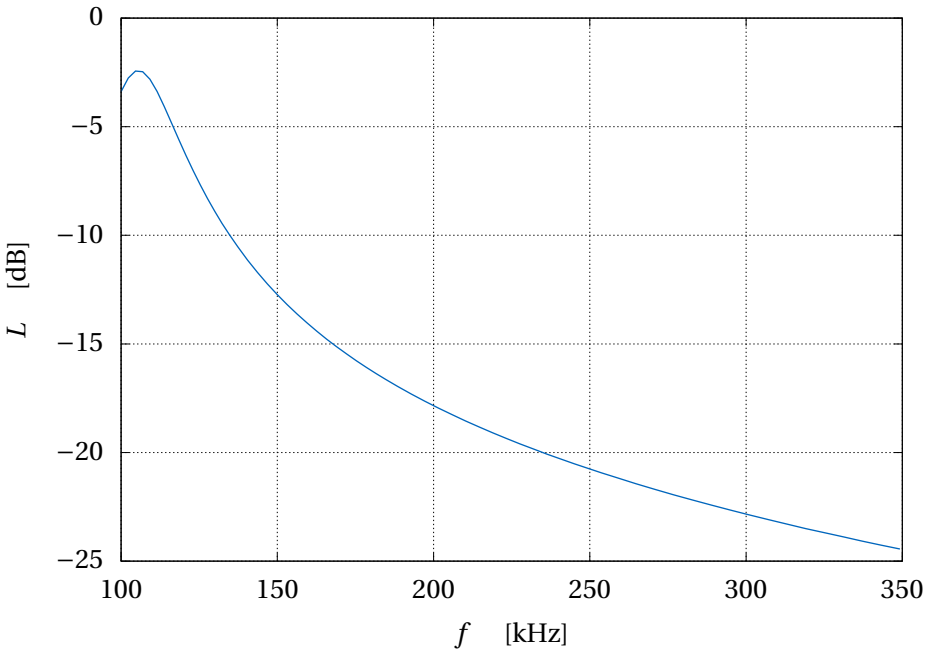

Figure A.8: Frequency response of the used filter

A.3 Simulated modulation responses

Note that the simulated data considers only amplitude power spectrum (absolute value of the FFT result), not phase spectrum. This means direction distinction is lost. More importantly, the sensitivity plot of modulation index response is positive, unlike real measurements, which are negative.

A.3.1 Frequency response

A.3.1.1 Maximum at f_λ

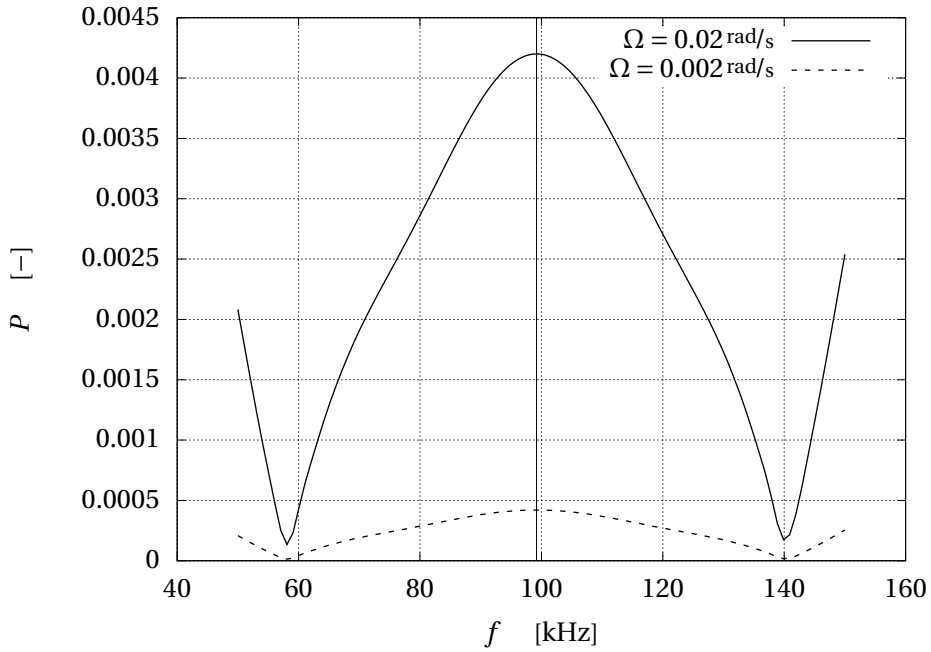

Figure A.9: Modulation frequency model response – small span: h = 2.4, f_λ = 99.2 kHz

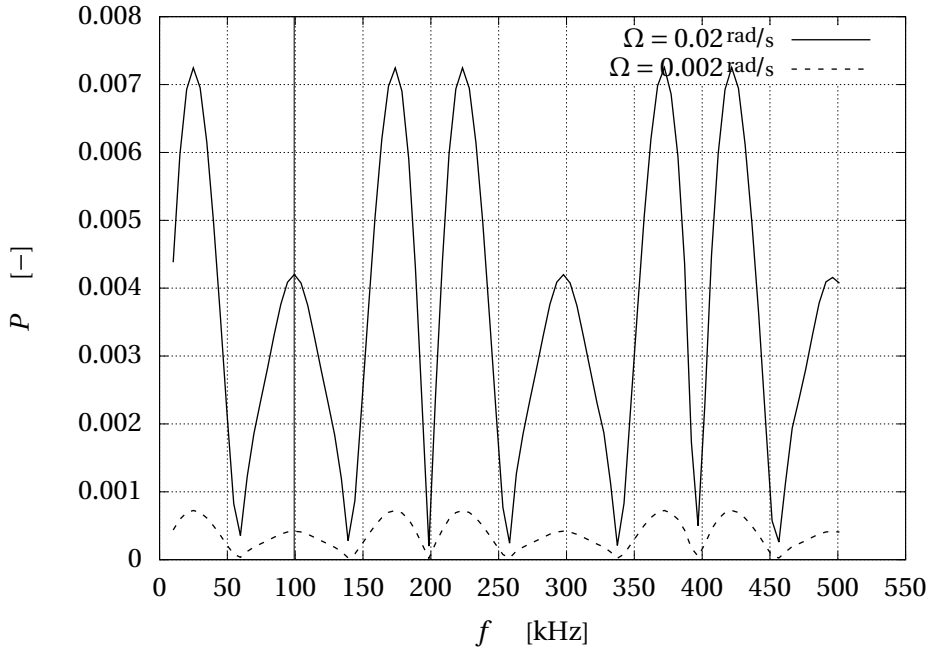

Figure A.10: Modulation frequency model response – large span: h = 2.4, f_λ = 99.2 kHz

A.3.1.2 Minimum at f_λ

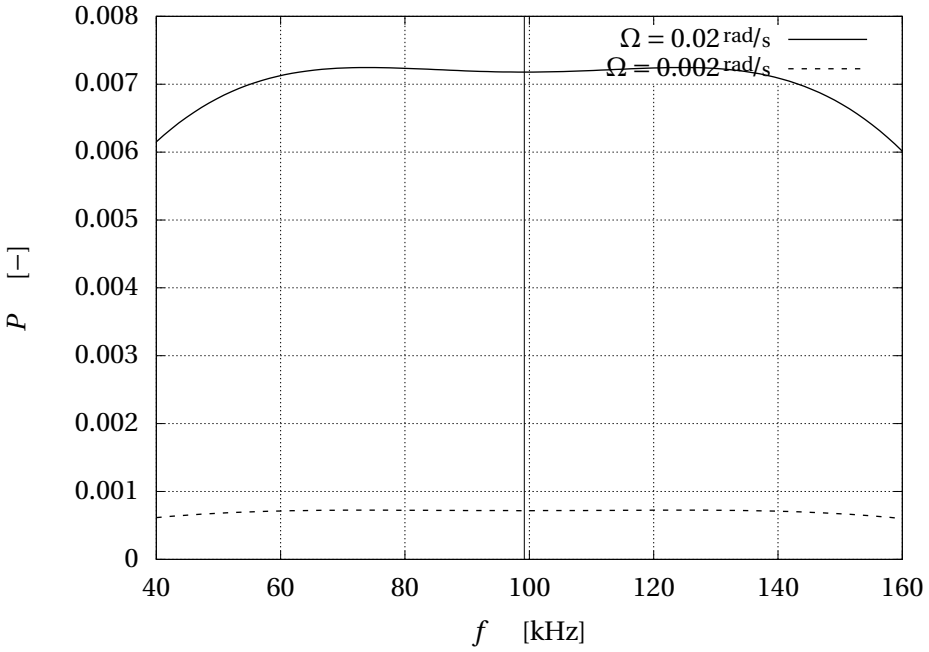

Figure A.11: Modulation frequency model response – small span: h = 1, f_λ = 99.2 kHz

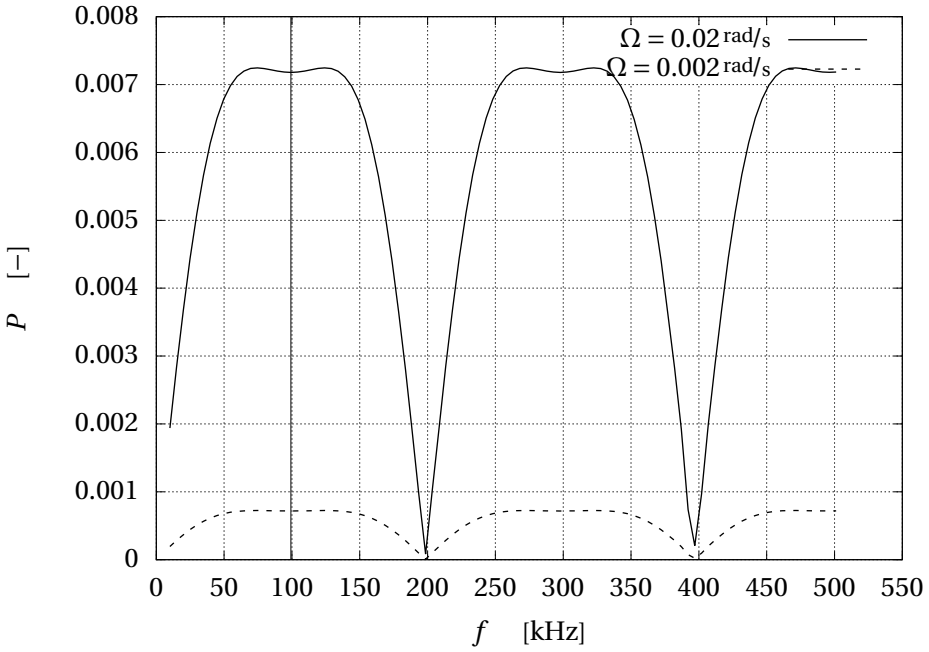

Figure A.12: Modulation frequency model response – large span: h = 1, f_λ = 99.2 kHz

A.3.2 Modulation index response

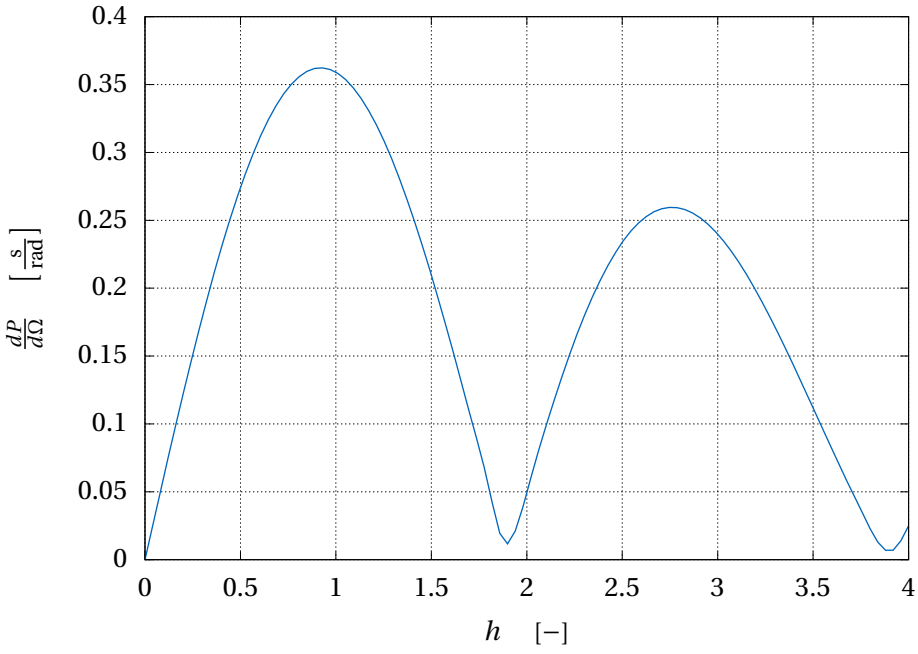

Figure A.13: Modulation index model response: $f_m = f_\lambda = 99.2$ kHz

A.4 Miscellaneous

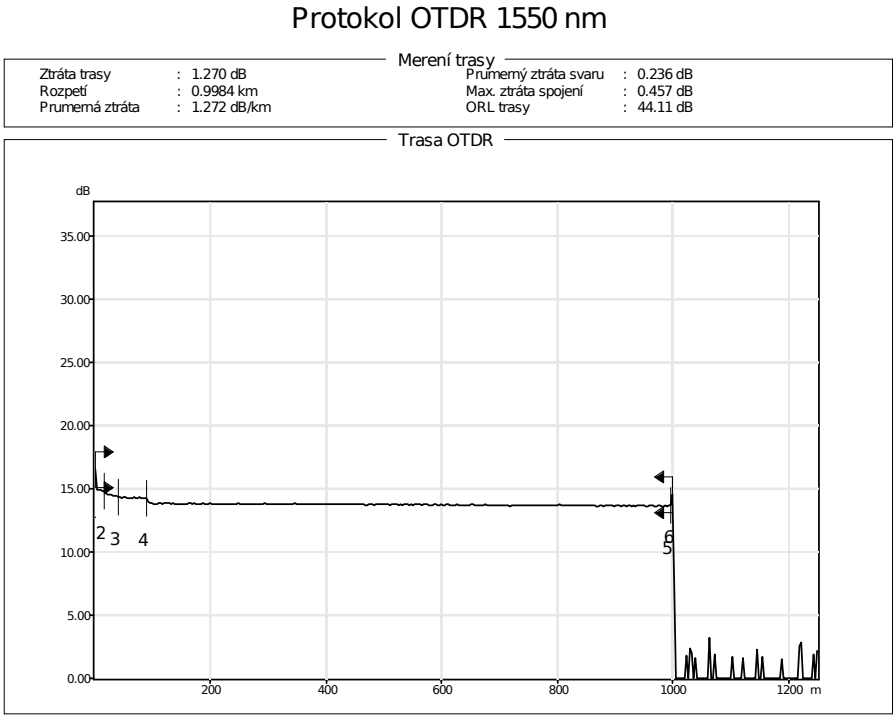

Figure A.14: SM spool – OTDR report

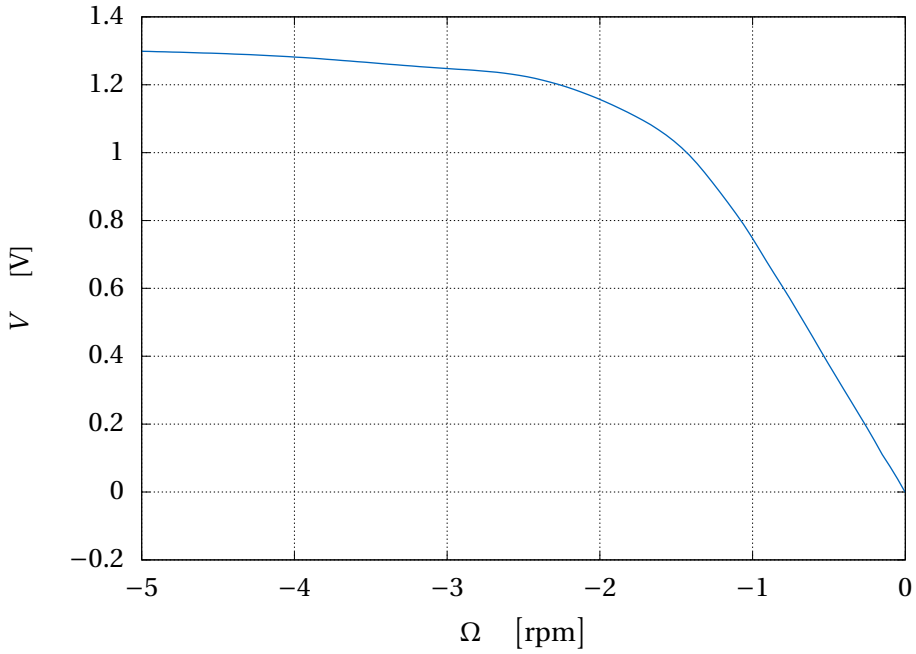

Figure A.15: PM setup response – high rotation rate

Appendix B

Supplementary mathematics

B.1 Modulation model derivation

From Sec. 1.1.2 beginning on p. 17:

$$\begin{aligned} v^+ &= \frac{\frac{c}{n}+\Omega r}{1+\frac{\Omega r}{cn}} \\ v^- &= \frac{\frac{c}{n}-\Omega r}{1-\frac{\Omega r}{cn}}. \end{aligned} \tag{B.1}$$

$$\begin{aligned} \tau^+ &= \frac{2\pi r N(cn+\Omega r)}{-c^2+\Omega^2 r^2} \\ \tau^- &= \frac{2\pi r N(-cn+\Omega r)}{-c^2+\Omega^2 r^2}. \end{aligned} \tag{B.2}$$

$$\begin{aligned} d^+ &= v^+\tau^+ = \frac{2\pi r N c(c+n\Omega r)}{c^2-\Omega^2 r^2} \\ d^- &= v^-\tau^- = \frac{2\pi r N c(c-n\Omega r)}{c^2-\Omega^2 r^2}. \end{aligned} \tag{B.3}$$

We need phase prescriptions for both waves:

$$\begin{aligned} \lambda^+ &= \frac{v^+}{c}\lambda_0 = \frac{(c+n\Omega r)\lambda_0}{cn+\Omega r} \\ \lambda^- &= \frac{v^-}{c}\lambda_0 = \frac{(c-n\Omega r)\lambda_0}{cn-\Omega r}, \end{aligned} \tag{B.4}$$

$$\begin{aligned} \phi^+ &= \frac{2\pi d^+}{\lambda^+} = \frac{2cL\pi(cn+\Omega r)}{\left(c^2-\Omega^2 r^2\right)\lambda_0} \\ \phi^- &= \frac{2\pi d^-}{\lambda^-} = \frac{2cL\pi(cn-\Omega r)}{\left(c^2-\Omega^2 r^2\right)\lambda_0} \end{aligned} \tag{B.5}$$

We will put the modulator at the entrance point of the positive (CCW) wave. This means the negative (CW) wave has its phase changed after traversing the Sagnac loop:

$$\begin{aligned} \phi_m^+ &= \phi^+ + h\sin(\omega_m t) = \frac{h\lambda_0\left(c^2-r^2\Omega^2\right)(\sin(t\omega_m))+2\pi cL(cn+r\Omega)}{\lambda_0\left(c^2-r^2\Omega^2\right)} \\ \phi_m^- &= \phi^- + h\sin(\omega_m(t+\tau^-)) = \frac{h\lambda_0\left(c^2-r^2\Omega^2\right)\left(\sin\left(\omega_m\left(\frac{L(cn-r\Omega)}{c^2-r^2\Omega^2}+t\right)\right)\right)+2\pi cL(cn-r\Omega)}{\lambda_0\left(c^2-r^2\Omega^2\right)}. \end{aligned} \tag{B.6}$$

Taking phase difference:

$$\Delta\phi_m = \left|\phi_m^+ - \phi_m^-\right| = \\ = \left| \frac{-h\lambda_0\left(c^2 - r^2\Omega^2\right)\left(\sin\left(\omega\left(\frac{L(cn-r\Omega)}{c^2-r^2\Omega^2} + t\right)\right)\right) + h\lambda_0\left(c^2 - r^2\Omega^2\right)(\sin(t\omega)) + 4\pi cLr\Omega}{\lambda_0\left(c^2 - r^2\Omega^2\right)} \right| \tag{B.7}$$

The sought relation is fraction of input power at the output port. As per equation 1.24 on page 21:

$$P_{out} = \frac{1}{4}\cos^2\left(\frac{\Delta\phi}{2}\right)P_{in} = \\ = \frac{1}{4}\cos^2\left| \frac{4cL\pi r\Omega + h\lambda_0(\sin(t\omega))\left(c^2 - r^2\Omega^2\right) - h\lambda_0\left(c^2 - r^2\Omega^2\right)\left(\sin\left(\omega\left(t + \frac{L(cn-r\Omega)}{c^2-r^2\Omega^2}\right)\right)\right)}{2\lambda_0\left(c^2 - r^2\Omega^2\right)} \right| P_{in} \tag{B.8}$$

Author: vidnepre@fel.cvut.cz
Electronic version includes:
– Source codes of the numerical computations
– Raw data from stability measurements
– Raw calculated Allan's variances

Set in Utopia and **Technika** typefaces
68 pages
34 figures

$$\Delta M_i^{-1} = -\alpha \sum_{n=1}^{N} D_i[n] \left[\sum_{j \in C[i]} F_{ji}[n-1] + Fext_i\left[n^{-1}\right] \right]$$